Theory of heavy-hole spin-echo dynamics

Xiaoya Judy Wang

Master of Science

Physics

McGill University

Montreal,Quebec

December 12, 2013

A thesis submitted to McGill University in partial fulfillment of the requirements of the degree of Master of Science in Physics.

ABSTRACT

In this work, we theoretically investigate hyperfine-induced effects on the spin-echo dynamics of a heavy hole in a quantum dot. We consider an in-plane applied magnetic field perpendicular to fluctuations arising from the hyperfine interaction, which drives the system into a motional averaging regime when the relevant (hole or nuclear) Zeeman energy scale exceeds the amplitude of hyperfine-induced fluctuations in the Overhauser field. For the parameters in Ref. [1], this system enters a motional averaging regime at moderate magnetic fields of the order of 1 T. In this regime, rapid spin precession about the external field effectively averages the out-of-plane fluctuations to zero, enabling the complete suppression of spin-echo envelope decay due to hyperfine coupling. We also predict the coherence dynamics to be strongly anisotropic, a property relevant to the discussion of electric-field-induced fluctuations currently limiting coherence times in single hole-spin experiments[2, 3]. More precisely, we find an alternative set of initialization and π-rotation axes which push the effects of electric-field-induced fluctuations out to very long timescales of the order of seconds for typical experimental parameters[2]. The anisotropy of this system also leads to counter-intuitive behaviour of the spin purity, an observable which quantifies the degree of spin-qubit polarization remaining after entangling with an environment for some time t. We find the spin purity to be maximally preserved when initializing along the hyperfine-induced fluctuations, in a superposition of Zeeman eigenstates. These results provide further evidence of the robustness of heavy-hole spin qubits, and

pave the way for prolonging hole-spin coherence by optimizing the geometry of the system.

ABRÉGÉ

Dans ce mémoire, nous étudions les effets de l'interaction hyperfine sur l'écho de spin d'un trou lourd localisé dans une boîte quantique. Nous considérons l'application d'un champ magnétique perpendiculaire aux fluctuations causées par l'interaction hyperfine, qui entraîne le système dans un régime de moyenne motionnelle lorsque l'énergie Zeeman pertinente (du trou ou des noyaux nucléaires) dépasse l'amplitude des fluctuations dans le champ de Overhauser. Avec les paramètres utilisés dans la Réf. [1], le régime de moyenne motionnelle est atteint pour un champ magnétique de l'ordre de 1 T. Dans ce régime, la précession rapide du spin autour du champ magnétique externe a l'effet d'une moyenne sur les fluctuations hyperfines, ce qui permet la suppression complète de la décroissance de l'enveloppe du signal de l'écho de spin. Nous prédisons aussi une anisotropie présente dans la dynamique de cohérence qui serait pertinente à la discussion des fluctuations du champ électrique, fluctuations qui limitent les temps de cohérence dans des expériences actuelles[2, 3]. Plus précisément, nous trouvons des directions d'initialisation et de rotation qui repoussent les effets des fluctuations électriques jusqu'à des échelles de temps de l'ordre de plusieurs secondes pour des paramètres expérimentaux typiques[2]. L'anisotropie du système est également responsable d'un comportement inattendu de la pureté du spin, qui quantifie la polarisation restante du qubit de spin suivant l'enchevêtrement avec un environnement pendant un temps t. Nous montrons que la pureté du spin est préservée au maximum pour une initialisation parallèle aux fluctuations hyperfines, dans une superposition

d'états propres Zeeman. Ces résultats fournissent une preuve supplémentaire du potentiel des qubits de spin de trou lourd, et permettent de prolonger leur cohérence en optimisant la géométrie du système.

CONTRIBUTION OF AUTHORS

Concerning the work presented in this thesis, I have performed all analytical calculations and numerical evaluations, except for Dr. Stefano Chesi's contribution described below, and have written most of the first draft for the article published in Phys. Rev. Lett. (PRL), all while under the guidance and supervision of Prof. Bill Coish. My collaborator Dr. Chesi developed the phenomenological electric-field-fluctuations model and was also responsible for its inclusion in the draft. All three authors of the paper contributed to improving the manuscript for submission to PRL, with Prof. Coish providing the vast majority of comments and suggestions. For the article in preparation, I have written the draft and updated it to its current version in accordance with Prof. Coish's comments and suggestions.

ACKNOWLEDGEMENTS

This thesis would not have been possible without the patient support and diligent guidance of my supervisor Bill Coish, who provided a constant supply of creative ideas and encouragement, and whose generosity, positivity and enthusiasm for physics are an inspiration, both in the workplace and in life. I am extremely grateful for a fruitful collaborative experience which has made me a better physicist and a more understanding person.

Furthermore, I have to thank Stefano for his timely and crucial contribution to our project, and Yingdan for her fabulous pizzas. I would also like to thank Ben, Stefano, Abhi, Félix, Perry, Saeed, and many others for their friendship and insightful/entertaining discussions about physics and everything else.

TABLE OF CONTENTS

CHAPTER 1
Introduction

The study of electron spins in solids has yielded numerous applications in electronics over the past few decades, most notably in magnetic memory devices and in spintronics. These applications utilize the macroscopic magnetization arising from the exchange interaction between a large number of spins, where quantum superpositions decay too quickly to be observed and the collective magnetization is represented by a classical vector [4]. However, the recent push to miniaturize electronics has led to the development of single-electron transistors, which contain a countable number of electrons. In semiconductor materials, further confinement down to nanometer lengthscales enables depletion down to zero electron in electrostatically delineated regions known as quantum dots [5], which can then be loaded with a single electron.

Single electrons in quantum dots currently form the basis for a potential implementation of quantum information processing. Such solid-state based implementations, while characterized by much shorter coherence times than atomic systems such as ion traps, are motivated by potentially greater scalability [6]. Since the original proposal by Loss and DiVincenzo in 1998, electron-spin quantum dot qubits have been extensively studied both theoretically and experimentally [7, 8]. However, it has been established that the coherence time for electron spins in III-V semiconductor quantum dots is typically limited by the strong hyperfine

interaction between the electron and the bath of surrounding nuclei, which leads to fast spin dephasing [9, 10, 11]. An alternative to using single electron spins is to use valence-band hole-spin states instead, which are believed to have longer coherence times due to their weaker hyperfine coupling strength and the anisotropic nature of their hyperfine interaction [12].

In this work, we present a theoretical investigation of the effects of the hyperfine interaction on hole-spin coherence. Among other results, we find the existence of a motional-averaging regime in which decay of hole-spin coherence is bounded. This regime can be reached in a moderate transverse magnetic field ($\sim$ 1T for the parameters in Fig. 2.2), whereby hyperfine-induced fluctuations in the hole-spin precession frequency are averaged out by rapid precession about the applied field [1].

The remainder of this chapter gives an overview of the main interactions governing single spins in quantum dots and of the resulting spin relaxation and decoherence mechanisms, followed by a discussion of the origin of heavy-hole states in III-V semiconductors and of the Ising form of the heavy-hole hyperfine Hamiltonian. In contrast to electron spin states, for heavy holes, the so-called 'flip-flop' terms are absent, leading to potentially longer coherence times for hole spins.

1.1 Confining and controlling single spins in quantum dots

Due to strong spatial confinement, energy levels inside quantum dots are quantized and can often be accurately described by the eigenenergies of a parabolic

well [13]. There exist many types of quantum dots, the most common and successful in quantum information processing being the gated lateral and self-assembled dots. Gated lateral quantum dots are fabricated by etching metallic gates on top of a heterostructure containing a 2D electron gas (2DEG), which forms at the interface between two semiconductor materials with different band gaps due to deformation of the energy bands [13], as shown in Fig. 1–1. Self-assembled quantum dots, which are commonly used in optical studies, may be fabricated through epitaxial growth of one semiconductor material on another with significantly different lattice constant. The strain due to lattice mismatch causes the deposited layer to bind to itself rather than to the underlying layer, leading to the formation of islands, or quantum dots [14].

While the techniques for indefinitely trapping single electrons and detecting single units of charge have become standard procedures [7], control over the spin degree of freedom is a recent development, having been achieved only in the past decade [7]. In an applied magnetic field, the spin-up and spin-down states can be taken to form a qubit, or two-level quantum system, necessary for quantum information processing. Experiments have now demonstrated arbitrary electron-spin rotation on the Bloch sphere [15] and control over two single-spin qubits [16], thus allowing in principle for any quantum operation [6]. However, maintaining coherence over long enough times to allow for many qubit rotations is still a challenge due to a combination of spin-orbit coupling and the electron-phonon interaction [17] as well as coupling to nuclear spins in the surrounding material [9, 10, 11]. Fluctuations in the environment can randomly flip the electron spin on

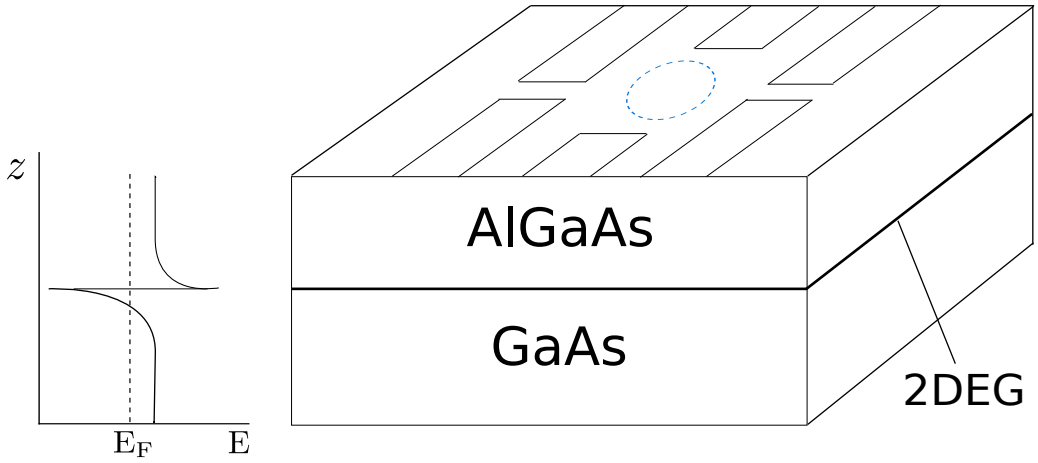

Figure 1–1: Gated lateral quantum dot: at the interface of two semiconductor materials with different band gaps (e.g. AlGaAs and GaAs), the energy levels are distorted such that a potential well is created which dips below the Fermi energy E_F, trapping electrons and forming a 2-dimensional electron gas (2DEG). Further confinement down to an area containing a single electron (blue circle) is achieved by depositing metallic gates on the top surface of the heterostructure, as shown by the rectangular strips.

a timescale characterized by the energy relaxation time T_1, and can cause loss of phase coherence on a timescale T_2 as well. The physical mechanisms responsible for these decoherence processes are summarized below.

1.2 Spin relaxation (T_1)

Electrons in a solid experience electric fields from charged atoms in the lattice, which can lead to different types of spin-orbit coupling. The two main forms of spin-orbit coupling for electrons in 2D systems are the Dresselhaus and Rashba spin-orbit interactions, which arise, respectively, from bulk inversion asymmetry (referring to the absence of a center of inversion) and structural inversion asymmetry (asymmetry of the potential well in Fig. 1–1) [18]. As an electron moves ballistically in the lattice, the rotation angle of its spin due to the spin-orbit coupling is only determined by the distance travelled l [19, 20]. It is therefore useful to define a quantity called the spin-orbit length λ_{SO}, which is the distance travelled for an electron spin to undergo a π-rotation due to spin-orbit interactions [20, 21]. In systems with lengthscales much shorter than λ_{SO}, such as quantum dots, the effects of spin-orbit interactions are suppressed [17, 19].

Quantum mechanically, spin-orbit coupling can be treated as a small perturbation to the discrete energy levels in the quantum dot. It mixes the unperturbed eigenstates, which are a product of orbital and spin degrees of freedom in the absence of the spin-orbit interaction [17]. The new eigenstates can couple to electric fields, leading to spin relaxation with the emission of an energy-conserving phonon [17, 22]. However, this coupling is suppressed in the ratio $\lambda_{\mathrm{dot}}/\lambda_{SO}$ for a quantum dot of size λ_{dot}. In this spin relaxation process, the emitted phonon energy

must match the Zeeman energy, and the phonon density-of-states vanishes at low energies in dimensions $d > 1$, leading to a further suppression of spin relaxation at low magnetic fields. Consequently, very long T_1 times in the μs to ms range have been observed experimentally [23, 24, 25], and values of T_1 exceeding 1 s have been measured at low magnetic fields [26]. For heavy holes, theoretical studies of spin relaxation through one-phonon [27] and two-phonon [28] processes have found values of T_1 comparable to those of electron spins [27, 28], in agreement with experiments [29, 30].

1.3 Hyperfine coupling and spin dephasing

The spin of an electron in a quantum dot will also couple to the surrounding nuclear spin bath. Due to the large number of nuclei in a typical dot, decoherence times induced by this hyperfine interaction are typically on the order of nanoseconds if no special effort is made to prolong the electron-spin lifetime [9, 10, 11]. The hyperfine coupling of a nuclear spin to an electron spin and orbital degrees of freedom can be written (in Gaussian CGS units) in the form [31, 12, 32]

$$H_{\rm hf} = 2\mu_B\mu_I \mathbf{I}\cdot\left[\frac{8\pi}{3}\delta(\mathbf{r})\mathbf{S} + \frac{\mathbf{L}}{r^3} - \frac{\mathbf{S}}{r^3} + 3\frac{\mathbf{r}(\mathbf{S}\cdot\mathbf{r})}{r^5}\right], \tag{1.1}$$

where μ_B is the Bohr magneton, μ_I is the nuclear magnetic moment, $\mathbf{I}$ is the nuclear spin operator, $\mathbf{S}$ and $\mathbf{L}$ are, respectively, the electron spin and orbital angular momentum operators, and $\mathbf{r}$ denotes the position of the electron relative to the nucleus. $H_{\rm hf}$ is the sum of a so-called Fermi contact term proportional to a delta function and an anisotropic interaction (the last three terms on the right of Eq.(1.1)).

The electron confined in a quantum dot will occupy a well-defined orbital ground state at temperatures T such that $kT < \Delta E$, where k is Boltzmann's constant and ΔE is the typical orbital spacing in the quantum dot. In this case, the effective contact hyperfine coupling in the orbital ground state is given by [31, 33]

$$H_{\text{chf}} = \sum_k A_k^{(e)} \mathbf{S} \cdot \mathbf{I}_k, \tag{1.2}$$

where $\mathbf{S} = \frac{1}{2}\sigma$ is the electron-spin operator (we have set $\hbar = 1$), $\mathbf{I}_k$ is the nuclear-spin operator, and the electron hyperfine constant for the nuclear spin at site k of isotope i_k is

$$A_k^{(e)} = A^{i_k} \nu_0 |\psi_0(\mathbf{r}_k)|^2, \tag{1.3}$$

with ν_0 the volume per nucleus and $\mathbf{r}_k$ denoting the location of the k^{th} nucleus within the lattice. In the envelope function approximation, the electron wavefunction can be written as the product of a Bloch amplitude periodic in the lattice and an envelope function $\psi_0(\mathbf{r})$ which varies slowly over the quantum dot [18]. The hyperfine coupling strength $A_k^{(e)}$ varies across the quantum dot since it depends on the nuclear isotope at site k and the magnitude squared of the electron envelope wavefunction, which drops off exponentially with distance from the center of the dot [8].

Bloch amplitudes for conduction-band electronic states have approximate s symmetry in III-V materials, whereas the valence-band Bloch amplitudes have approximate p symmetry [12]. The anisotropic hyperfine coupling vanishes for the spherically symmetric s-orbital states, but is finite for states of higher angular momentum, such as the p-orbital states in the valence band [33]. After projecting

onto a $p-, d-$, or $f-$ orbital state and rotating to site-dependent principal axes such that the off-diagonal elements in the hyperfine tensor vanish, the anisotropic hyperfine interaction can be written as [33]

$$H_{\text{ahf}} = \sum_k \sum_\alpha A_k^{\alpha\alpha} S^\alpha I_k^\alpha, \tag{1.4}$$

where $\alpha = x, y, z$ and the coupling constants $A_k^{\alpha\alpha}$ depend strongly on the symmetry of the electronic wavefunction [33, 8]. For electrons in s-type orbitals, such as in the conduction band of III-V semiconductors, only the contact hyperfine interaction is finite. On the other hand, holes in p-type orbitals in the valence band have wavefunctions that vanish at nuclear sites, leaving only the weaker anisotropic interaction [12]. Both types of hyperfine coupling include a longitudinal term which preserves the z-projection of the electron spin ($\propto I_z S_z$) and in-plane components ($\propto I_x S_x + I_y S_y = \frac{1}{2}(I_+ S_- + I_- S_+)$), the so-called flip-flop terms, which can flip the electron spin when a nuclear spin flips. As will be discussed in section 1.5 below, the flip-flop terms for heavy-hole spins vanish in the presence of strong confinement along z, resulting in an Ising ($\propto S_z I_z$) coupling [12] and leading to potentially longer coherence times for heavy-hole spins, relative to electron spins.

The hyperfine interaction of Eq.(1.2) can alternatively be thought of as the coupling of an electron spin to an effective magnetic field known as the nuclear Overhauser field $\mathbf{h}$, defined by

$$\mathbf{h} = \sum_k A_k \mathbf{I}_k. \tag{1.5}$$

Since the Overhauser field is composed of $10^4 - 10^6$ randomly oriented nuclear spins, the electron spin experiences a fluctuating precession frequency and decoheres very rapidly. These fluctuations can be either statistical (varying from one experiment to the next) or quantum in nature. Additionally, interactions within the nuclear spin bath give rise to a slow evolution of the Overhauser field, the most important of which is the nuclear dipolar interaction [34]. The nuclear dipole-dipole coupling can cause neighbouring nuclear spins to flip, thus exchanging angular momentum and leading to fluctuations in the Overhauser field, which in turn results in an electron-spin decay timescale of $\tau_{dd} \sim 10\mu$s[35]. However, since the hyperfine-induced dephasing studied here is characterized by timescales on the order of $\lesssim 100$ns, the inter-nuclear interactions can be safely neglected.

1.4 Spin-echo decay

Spin-echo techniques can significantly extend coherence times by removing dephasing due to fluctuations in the electron spin precession frequency which are effectively static. We denote by T_2 the spin-echo decay time, while T_2^* characterizes the free-induction decay time when no special effort is made to extend the spin lifetime. As illustrated in Fig. 1–2, the spin-echo process involves a π-pulse which rotates the electron spin by 180° at $t = \tau$, thereby reversing the evolution from $t = \tau$ to $t = 2\tau$ and leading to a spin refocusing at $t = 2\tau$ provided the spin experiences a static unknown field. While the simple Hahn (single-pulse) spin-echo sequence of Fig. 1–2 only eliminates static fluctuations, more complicated pulse sequences based on dynamical decoupling can further decouple the system from the evolving environment through a series of successive stroboscopic spin flips.

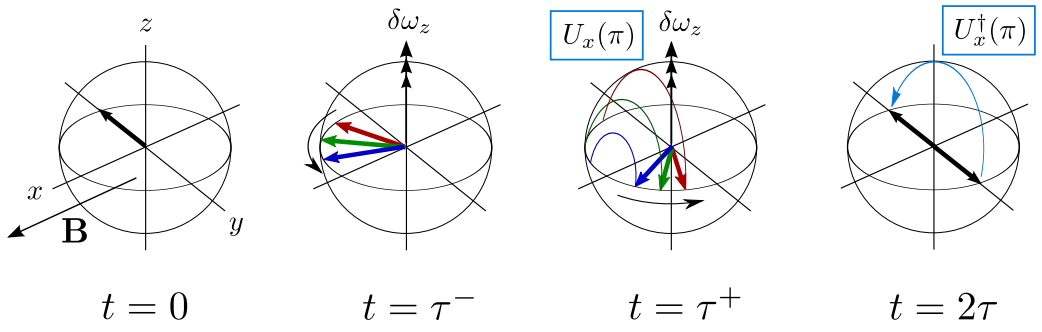

Figure 1–2: Hahn echo sequence with π-rotation $U_x(\pi)$ about $\hat{x}$, which reverses dephasing from hyperfine-induced fluctuations $\delta\omega_z$ in the Overhauser field along $\hat{z}$. The applied magnetic field is $\mathbf{B} = B\hat{x}$, and in this figure we assume an in-plane hole g-factor $g_\perp \simeq 0$ for simplicity such that there is no precession of the hole spin about $\hat{x}$.

In particular, the Uhrig dynamical decoupling (UDD) sequence has been shown to optimize the number of spin flip operations to achieve maximal decoupling efficiency in certain specific types of environment and has been used to improve coherence times by up to 25 times [36, 37].

1.5 Heavy-hole states in III-V semiconductors

Unlike electrons in the conduction band whose orbital states are s-like, holes in the valence band in bulk III-V semiconductors have approximately p-like orbital states with angular momentum $l = 1$ [12]. The strong spin-orbit interaction thus splits the electronic states in the valence band into states with total angular momentum $j = \frac{1}{2}$ and $j = \frac{3}{2}$ [18], according to the rules of addition of angular momentum. An accurate description of the band structure requires the application of Bloch's theorem to solve the Schrödinger equation for electrons in a periodic crystal lattice. For nanostructures, corrections to the bulk solutions can be found from the $\mathbf{k} \cdot \mathbf{p}$ method and the envelope function approximation, which allows for

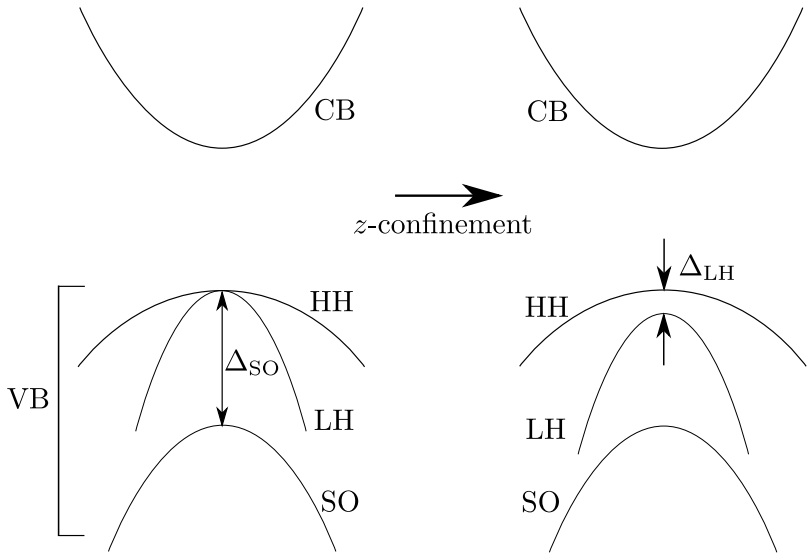

Figure 1–3: Band structure of III-V semiconductors in bulk (left) and in 2D quantum wells (right) near the fundamental gap between the conduction band (CB) and the valence band (VB). The valence band further splits into the heavy-hole (HH), light-hole (LH), and split-off (SO) bands, the last of which is offset by the spin-orbit gap Δ_{SO} at $k = 0$. Strong confinement in 2D quantum wells creates a splitting Δ_{LH} at $k = 0$ between the HH and LH bands due to their different effective masses.

accurate solutions in the presence of arbitrary electric or magnetic fields that vary slowly on atomic length scales [18]. A qualitative schematic of the resulting band diagram is drawn in Fig. 1–3, showing the three distinct valence sub-bands. The $j = \frac{1}{2}$ and $j = \frac{3}{2}$ bands are separated in energy by the spin-orbit gap Δ_{SO} at $k = 0$, while the $j = \frac{3}{2}$ band splits into the heavy hole (HH) and light hole (LH) bands corresponding to states with z-projection of angular momentum $J_z = \pm\frac{3}{2}$ and $J_z = \pm\frac{1}{2}$, respectively [18]. The terms heavy hole and light hole refer to their effective masses for motion perpendicular to the growth axis (the z-axis in Fig. 1–1). We have assumed that the growth direction is aligned with the [001]

crystallographic axis in Fig. 1–3. In quasi-2D systems with strong confinement along the growth direction, a further splitting at $k = 0$ develops between the HH and LH bands, known as the HH-LH splitting Δ_{LH} [18]. In GaAs, Δ_{LH} has been estimated to be $\simeq 100$ meV for a quantum well with a height of 5 nm [12], which is many orders of magnitude larger than the hyperfine coupling and allows for a well-defined two-level system in the HH subspace.

The hyperfine interaction of Eq.(1.1) is a vector operator in the electron spin and orbital angular momentum space, or equivalently, a tensor operator of rank 1. According to the Wigner-Eckart theorem, which states that a rank-n operator can couple states which differ at most by n units of angular momentum, the hyperfine interaction must therefore have vanishing off-diagonal elements in the HH basis, since the spin-up and spin-down states differ by three units of angular momentum. This results in a simple Ising hyperfine coupling [12]:

$$H_{\mathrm{hf}} = \sum_k A_k S_z \cdot I_k^z, \tag{1.6}$$

where $\mathbf{S}$ is now the pseudospin-1/2 operator in the heavy-hole ($J_z = \pm 3/2$) subspace such that $S_z = \frac{1}{2}\left(\left|+\frac{3}{2}\right\rangle\left\langle+\frac{3}{2}\right| - \left|-\frac{3}{2}\right\rangle\left\langle-\frac{3}{2}\right|\right)$ and A_k is the heavy-hole hyperfine coupling for the nuclear spin at site k. The average hyperfine coupling has been estimated and confirmed experimentally to be $A = \sum_k A_k \sim 13\mu$eV in GaAs, about 10 times weaker than the average electron hyperfine coupling $A^{(e)} = \sum_k A_k^{(e)}$[12].

Several sources of non-Ising corrections to $H_{\rm hf}$ have been shown to be small for a quantum dot with negligible strain [12]. Processes involving virtual transitions via the light-hole sub-band are suppressed by $A/\Delta_{LH} \ll 1$ [12], hybridization with the conduction, light-hole and split-off bands result in small effects of order $0.01A$ [12], and corrections due to a finite dot thickness come into play on a time scale $\gtrsim 10\mu$s [38].

Nuclei with spin $I > 1/2$ also have a finite electric quadrupole moment which can couple to electric-field gradients arising from the local electric fields of electrons in states with finite orbital angular momentum. Provided there are no strain-induced electric field gradients, the typical size of the quadrupole splitting for a single ^{69}Ga nuclear spin coupled to a valence-band heavy hole has been estimated to be $|E_Q| \simeq 0.01\mu$eV [8], much smaller than the hyperfine coupling strength.

However, rotational symmetry is in principle broken by the lattice, which could lead to further corrections from non-p-like (higher-orbital) contributions to the Bloch amplitudes[39]. The presence of non-Ising terms from this hybridization has yet to be experimentally established.

Recent and ongoing experiments have demonstrated the coherence of hole-spin states through coherent population trapping, where initialization of the spin qubit is achieved by resonantly driving the system into an optically dark state [40]. The magnitude of the hyperfine constant has been measured [41, 42] and found to agree with predictions [12] up to a sign difference attributed to atomic d-like orbital contributions to the Bloch amplitudes [39]. Coherent optical control of hole-spin

qubits has also been implemented [2, 43, 3], including a Hahn-echo sequence [2] which enables measurements of both T_2^* and T_2 times.

Existing theoretical work has determined the strength [32] and the Ising form [12] of the heavy-hole hyperfine Hamiltonian, and studied non-Ising corrections due to hybridization with other bands [38] as well as their effects on decoherence times [44]. Although the hyperfine interaction is the limiting term for coherence of single electron spins, we show here that decay in the heavy-hole spin-echo envelope can be completely suppressed if the strength of the in-plane magnetic field exceeds the amplitude of hyperfine-induced fluctuations.

1.6 Outline of manuscript chapters

In this thesis, we calculate the hyperfine-induced coherence dynamics of a heavy hole subject to spin echo, assuming a flat, unstrained quantum dot. In an applied magnetic field, the rapid hole and nuclear Zeeman precession allows for an accurate description of the dynamics via an average-Hamiltonian theory, which is valid when the amplitude of fluctuations from hyperfine coupling are small relative to the relevant Zeeman energy.

The body of this thesis consists of two manuscripts, which together document the procedures and results developed throughout this work. Each chapter is preceded by a brief introduction which summarizes the key results and places them in context relative to the overall progress made in the course of this project. Chapter 2 focuses on the hole-spin component lying along the in-plane external field to demonstrate that moderate values of the magnetic field ($\gtrsim$ 1T for the parameters in Fig. 2.2) can enable the complete suppression of hyperfine-induced

decay in the spin-echo envelope function. In Chapter 3, we examine all spin components and find that the spin purity is best preserved for initialization along the axis parallel to hyperfine fluctuations (perpendicular to the external field), even though one could expect highest spin purity when initializing along a Zeeman eigenstate. We therefore conclude that the hyperfine interaction does not limit hole-spin coherence times at moderate magnetic fields, and that optimizing the geometry (initialization and π-rotation axes) of the system can further suppress loss of spin-qubit polarization.

Introduction to chapter 2

In chapter 2, we calculate the spin-echo dynamics of a heavy hole in a quantum dot by developing an approximation scheme based on an average-Hamiltonian theory known as the Magnus expansion. We show that a moderate in-plane magnetic field ($\sim$ 1T for the parameters in Fig. 2.2) can lead to motional averaging, whereby fluctuations transverse to the applied magnetic field are averaged out by rapid spin precession. The hyperfine interaction is therefore not the limiting factor for hole-spin coherence in the regime of motional averaging. We also find that hole spin-echo decay is highly anisotropic, depending on both the choice of initialization and of π-rotation axes. In particular, we show that the effects of electric-field fluctuations reported in a recent spin-echo experiment [2] can be highly suppressed in an alternative geometry. In chapter 3, we will offer a more generalized discussion of the consequences of anisotropy in this system.

CHAPTER 2
Spin-echo dynamics of a heavy hole in a quantum dot

[X. J. Wang, Stefano Chesi, and W. A. Coish, Phys. Rev. Lett. 109, 237601 (2012).]

2.1 Introduction

Electron spins in solid-state systems provide a versatile and potentially scalable platform for quantum information processing [6, 7]. This versatility often comes at the expense of complex environmental interactions, which can destroy quantum states through decoherence. Many theoretical and experimental studies have now established that the coherence times of electron spins in quantum dots [9, 10, 15, 45], bound to donor impurities [34, 46], and at defect centers [47] are typically limited by the strong hyperfine interaction with surrounding nuclear spins [7, 8]. Heavy-hole spin states in III-V semiconductor quantum dots have emerged as a platform that could mitigate the negative effects of the hyperfine interaction. Due to the p-like nature of the valence band in III-V materials, the contact interaction vanishes for hole spins, leaving only the weaker anisotropic hyperfine coupling [12, 48]. Moreover, the anisotropy of this interaction in two-dimensional systems should allow for substantially longer dephasing times in a magnetic field applied transverse to the quantum-dot growth direction [12, 8].

Recent experiments have measured hyperfine coupling constants for holes [41, 49, 42], as well as spin-relaxation (T_1) [30] and free-induction decay times, T_2^*,

through indirect (frequency-domain) [40] and direct (time-domain) studies [2]. Coherent optical control has now been demonstrated for hole spins in single [2, 50] and double quantum dots [3]. This technique has been used to implement a Hahn spin-echo sequence [2] giving an associated spin-echo decay time, $T_2 \sim 1\,\mu$s. The T_2 value reported in Ref. [2] has been attributed to device-dependent electric-field fluctuations, rather than the intrinsic hyperfine interaction. Motivated by these recent experiments, here we present a theoretical study of heavy-hole spin-echo dynamics with an emphasis on identifying the optimal conditions for extending coherence times. In particular, we show that dephasing due to electric-field fluctuations, as proposed in Ref. [2], is dramatically suppressed in an alternate geometry considered here. Moreover, in contrast with the case of electron spins, we find that hole spins can enter a motional-averaging regime in a moderate magnetic field. In this regime, coherence is no longer limited by the hyperfine interaction, solidifying the potential for long-lived hole-spin qubits.

We consider a heavy-hole (HH) spin interacting with nuclear spins in a flat quantum dot with weak strain (see Fig. 2–1). The HH spin is then described with

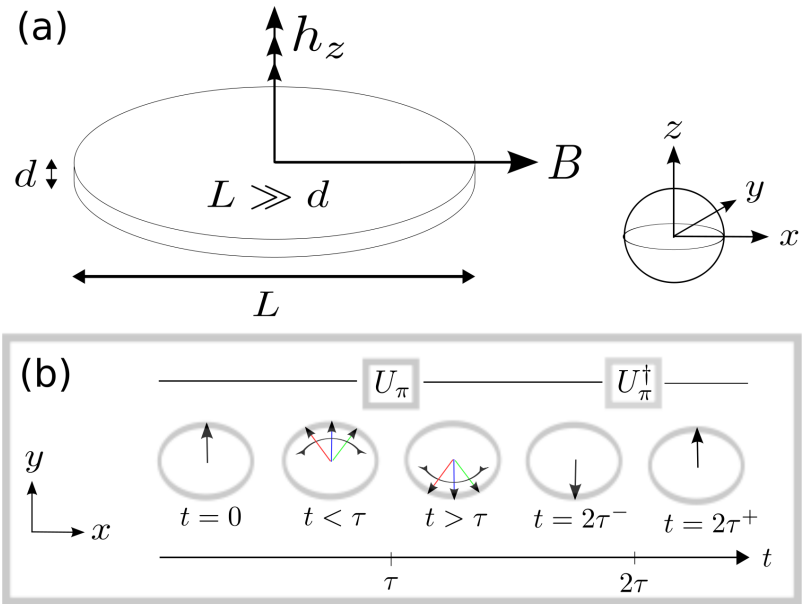

Figure 2–1: (Color online) (a) Quantum-dot geometry, with nuclear field h_z and magnetic field $\mathbf{B} = B\hat{x}$. For unstrained and flat quantum dots ($d \ll L$), $\gamma_H = g_\perp \mu_\mathrm{B} \simeq 0$ and $h_{x,y} \simeq 0$ [12, 38, 44]. (b) Hahn echo sequence. Two π-rotations (U_π and $U_\pi^\dagger$, taken here about the x-axis) are applied at $t = \tau$ and 2τ, to refocus the HH spin.

the following Hamiltonian [1] (setting $\hbar = 1$),

$$H = H_Z + h_z S_z, \quad H_Z = -\gamma_H B S_x - \sum_k \gamma_{i_k} B I_k^x, \tag{2.1}$$

where $\mathbf{S} = \boldsymbol{\sigma}/2$ is a pseudospin-1/2 operator in the two-dimensional ($J^z = \pm 3/2$) HH subspace and $\mathbf{I}_k$ the nuclear spin at site k. H_Z gives the hole- and nuclear-Zeeman interactions for an in-plane magnetic field $\mathbf{B} = B\hat{x}$ [see Fig. 2–1(a)]. γ_{i_k} is the gyromagnetic ratio of isotope i_k at site k having total spin I_{i_k}. The hole gyromagnetic ratio is $\gamma_H = g_\perp \mu_B$, with $g_\perp$ the in-plane g-factor for a dot with growth axis along [001] and μ_B the Bohr magneton. The hyperfine interaction [12, 8] is expressed in terms of the Overhauser operator, $\mathbf{h} = \sum_k A_k \mathbf{I}_k$. The coupling constants, A_k, are given by $A_k = A^{i_k} v_0 |\psi(\mathbf{r}_k)|^2$, with A^i the hyperfine constant for isotope i, v_0 the volume occupied by a single nuclear spin, and $\psi(\mathbf{r}_k)$ the HH envelope wavefunction. When the isotopes are distributed uniformly across the dot, we define the average $A = \sum_k A_k \simeq \sum_i \nu_i A^i$, with ν_i the isotopic abundance. In this case, and for a Gaussian envelope function in two dimensions, $A_k \simeq (A/N) e^{-k/N}$ [11] with $N = 10^4 - 10^6$ a typical number of nuclear spins within a quantum-dot Bohr radius. The ratio of $|A|$ to the strength of the hyperfine coupling of electrons, $|A^{(e)}|$, has been estimated theoretically [12] in GaAs and

[1] In Eq. (2.1), we neglect terms $\sim \quad h_{x,y}$, and nuclear quadrupole coupling. This is valid for a flat quantum dot with weak strain [12, 38, 44, 51]. The nuclear dipolar interaction may also influence the Hahn-echo decay of an electron spin on a timescale $\tau_{dd} \sim 10\,\mu\text{s} \propto 1/\sqrt{A^{(e)}}$ [35]. Since $|A| < |A^e|$, we expect τ_{dd} to be still longer for holes, beyond the times considered here.

confirmed experimentally [41, 42] in InGaAs and InP/GaInP to be $|A/A^{(e)}| \sim 0.1$. For simplicity, we will evaluate numerical estimates with a single averaged value $|A^i| \simeq |A| \simeq 13\,\mu$eV [12, 8] and ν_i, γ_i appropriate for $In_{0.5}Ga_{0.5}As$.

2.2 Spin echo

Under the action of Eq. (2.1), spin dephasing results from fluctuations in h_z. Provided these fluctuations remain static on the timescale of decay of the hole spin, this source of decay can be removed via a Hahn echo [see Fig. 2–1(b)]. The process is better analyzed in the interaction picture with respect to H_Z,

$$\tilde{H}(t) = \tilde{h}_z(t)\tilde{S}_z(t), \tag{2.2}$$

where, for any $\mathcal{O}$, $\tilde{\mathcal{O}}(t) = e^{iH_Z t}\mathcal{O}e^{-iH_Z t}$. In particular, $\tilde{h}_z(t) = \sum_k A_k[I_k^z \cos(\gamma_{i_k} Bt) - I_k^y \sin(\gamma_{i_k} Bt)]$ and $\tilde{S}_z(t) = [S_z \cos(\gamma_H Bt) - S_y \sin(\gamma_H Bt)]$. The time-evolution operator after a time 2τ is then given by:

$$\tilde{U}(2\tau) = \mathcal{T} e^{-i\int_0^{2\tau} dt \tilde{H}_e(t)}. \tag{2.3}$$

Here, $\mathcal{T}$ is the time-ordering operator and the modified echo Hamiltonian,

$$\tilde{H}_e(t) = \begin{cases} \tilde{H}(t) & 0 \le t < \tau, \\ \sigma_\alpha \tilde{H}(t) \sigma_\alpha & \tau \le t \le 2\tau, \end{cases} \tag{2.4}$$

takes into account π_α-pulses (π-rotations about $\alpha = x, y, z$). As seen in Eq. (2.4), π_x-pulses (but in general not π_y, π_z) have the beneficial effect of inverting the sign of the Hamiltonian, $\tilde{H}(t) \to -\tilde{H}(t)$, in the interval $\tau \le t \le 2\tau$. Provided $\tilde{H}(t)$ is approximately static over the interval $0 < t < 2\tau$, this will induce time-reversed

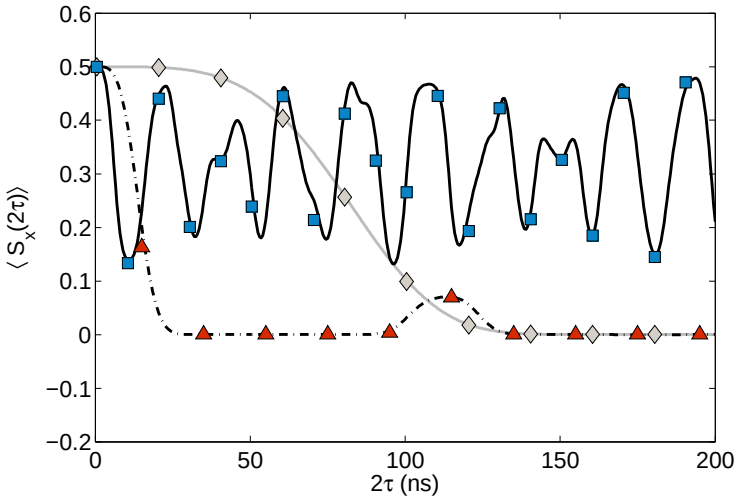

Figure 2–2: (Color online) Exact analytical spin-echo decay with $B = 50\,\mathrm{mT}$ (solid gray), $B = 2\,\mathrm{T}$ (dash-dotted), and $B = 10\,\mathrm{T}$ (solid black), corresponding to the regimes $B \lesssim A/(\gamma_i\sqrt{N})$, $B \simeq A/(\gamma_i\sqrt{N})$, and $B \gtrsim A/(\gamma_i\sqrt{N})$, respectively. Markers show the approximate form, Eq. (2.7). We have chosen $\langle S_x(0)\rangle = 1/2$, $N = 10^4$, $\gamma_H = g_\perp\mu_B = 0$, and γ_i from Table 1 of Ref. [8].

dynamics for $\tau \le t \le 2\tau$, refocusing decay at the time 2τ. For this reason, unless otherwise specified, we will focus in the following discussion on a geometry with the magnetic field along $\hat{x}$ and π_x-pulses. We will contrast this analysis later with an alternate geometry relevant to recent experiments.

2.3 Vanishing $g_\perp$

We first consider the limit $\gamma_H = g_\perp\mu_\mathrm{B} = 0$ in Eq. (2.1). The dynamics we find in this limit will be a good description whenever $\gamma_H < \gamma_i$, corresponding to $g_\perp < 10^{-3}$ ($g_\perp < 5\times10^{-3}$ has been reported in 2D wells [52]). This limit considerably simplifies the theoretical analysis and allows for an exact solution: H becomes block diagonal in the eigenbasis of S_z and, in each block, the eigenstates

are obtained after rotating I_k^z-eigenstates by an angle $\theta_k = \pm \arctan(2\gamma_{i_k} B/A_k)$ about $\hat{y}$. Representative results of the exact evolution of $\langle S_x(2\tau)\rangle$ are shown in Fig. 2.2. The spin-echo signal has a remarkable dependence on the magnetic field: there is a clear transition from a low-field regime, where the decay time decreases with increasing B, to a high-field regime, where there is no decay, only modulations of the echo envelope.

To give physical insight, we have developed an analytical approximation scheme based on the Magnus expansion. The Magnus expansion is an average-Hamiltonian theory typically applied to periodic and rapidly oscillating systems [53]. This scheme is suggested by the oscillating terms in Eq. (2.2), and will allow us to analyze the more general problem with $\gamma_H \neq 0$. In the Magnus expansion, we assume the evolution operator, Eq. (2.3), can be written as $\tilde{U}(2\tau) = e^{-iH_M(2\tau)} = e^{-i\sum_{i=0}^{\infty} H^{(i)}(2\tau)}$. The i^{th}-order term, $H^{(i)}(t)$, is found using standard methods [53]. Each higher-order term in the Magnus expansion contains one additional integral over time. Oscillating terms are therefore suppressed by a factor of order $\|\tilde{H}\|/\omega$, with ω the typical oscillation frequency. The leading-order term is $H^{(0)}(t) = \overline{H(t)}t$, where $\overline{H(t)}$ is simply the average of $\tilde{H}_e(t)$ over an interval t. The spin components S_α ($\alpha = x, y, z$) are then given by:

$$\left\langle S_\alpha(2\tau)\right\rangle = \left\langle \tilde{U}^\dagger(2\tau)\tilde{S}_\alpha(2\tau)\tilde{U}(2\tau)\right\rangle = \left\langle e^{iL_M(2\tau)}\tilde{S}_\alpha(2\tau)\right\rangle, \tag{2.5}$$

where $L_M(t)$ is defined by $L_M(2\tau)\mathcal{O} = \left[H_M(2\tau), \mathcal{O}\right]$ and $\langle\mathcal{O}\rangle = \mathrm{Tr}\{\mathcal{O}\rho\}$. The initial state $\rho = \rho_S \otimes \rho_I$ is assumed to describe a product of the hole-spin (ρ_S)

	$\gamma_H \gg \gamma_i$	$\gamma_H \ll \gamma_i < \frac{A}{B\sqrt{N}}$	$\gamma_H \ll \frac{A}{B\sqrt{N}} < \gamma_i$
ω	$\sim B\gamma_H$	$\sim B\gamma_i$	$\sim B\gamma_i$
$\delta\omega_{\rm rms}$	$\sim A/\sqrt{N}$	$\sim A/N$	$\sim A/N$
$\tau_{\rm max}$	$\sim \omega/\delta\omega_{\rm rms}^2$	$\sim \frac{1}{A}(\omega/\delta\omega_{\rm rms})^3$	$\sim \omega/\delta\omega_{\rm rms}^2$

Table 2–1: The Magnus expansion will generally reproduce the correct dynamics for $\delta\omega_{\rm rms}/\omega < 1$ and $\tau < \tau_{\rm max}$, with ω, $\delta\omega_{\rm rms}$, and $\tau_{\rm max}$ given above in three regimes.

and nuclear-spin (ρ_I) density matrices, where the nuclear spins are in an infinite-temperature thermal state. For $N \gg 1$ uncorrelated nuclear spins, the central-limit theorem gives nearly Gaussian fluctuations, resulting in

$$\left\langle e^{iL_M(2\tau)}\tilde{S}_\alpha \right\rangle \simeq \left\langle \exp\Big\{ -\frac{1}{2}\big\langle L_M^2(2\tau)\big\rangle_I \Big\}\tilde{S}_\alpha \right\rangle_S , \tag{2.6}$$

where we define $\langle L_M^2(t)\rangle_I \mathcal{O}_S = {\rm Tr}_I\{(L_M^2(t)\mathcal{O}_S)\rho_I\}$ and $\langle\mathcal{O}\rangle_S = {\rm Tr}_S\{\mathcal{O}\rho_S\}$.

At high B, rapid oscillations in $\tilde{H}(t)$ allow us to keep only the leading term: $L_M(2\tau)\mathcal{O}_S \simeq L^{(0)}(2\tau)\mathcal{O}_S = [H^{(0)}(2\tau), \mathcal{O}_S]$. Setting $\gamma_H = 0$, as appropriate for Fig. 2.2, and with the help of $\sum_k' A_k^2 \simeq \nu_i A^2/(2N)$ (where the prime restricts the sum to nuclei of isotopic species i), we obtain:

$$\frac{\langle S_x(2\tau)\rangle}{\langle S_x(0)\rangle} \simeq \exp\left[-\sum_i \frac{4\nu_i A^2 I_i(I_i+1)}{3N(\gamma_i B)^2} \sin^4\left(\frac{\gamma_i B\tau}{2}\right)\right]. \tag{2.7}$$

As seen in Fig. 2.2, Eq. (2.7) (markers) reproduces the exact dynamics very well. The precise conditions for the validity of the Magnus expansion will be given below.

The simple form of Eq. (2.7) enables us to understand why the behavior of $\langle S_x(2\tau)\rangle$ changes as B is increased. For $B \ll A/(\gamma_i\sqrt{N})$ (gray solid line in

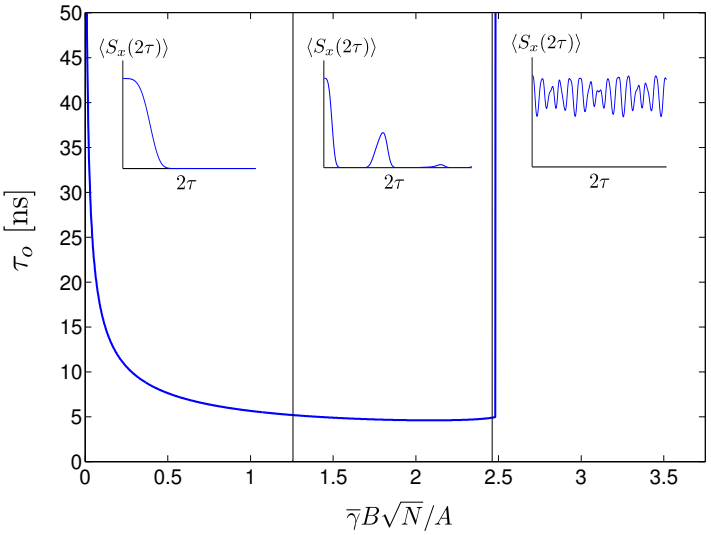

Figure 2–3: (Color online) Decay time, τ_0, vs. B. Here, $\overline{\gamma} = \sum_i \nu_i\gamma_i$ and parameters are as given in the caption of Fig. 2.2. Insets: typical $\langle S_x(2\tau)\rangle$ in each of the three regions: $\overline{\gamma}B\sqrt{N}/A \ll 1$, $\overline{\gamma}B\sqrt{N}/A \sim 1$, and $\overline{\gamma}B\sqrt{N}/A \gg 1$.

Fig. 2.2), a short-time expansion of Eq. (2.7) gives $\langle S_x(2\tau)\rangle \simeq \langle S_x(0)\rangle\,(1-(\tau/\tau_0)^4) \simeq \langle S_x(0)\rangle e^{-(\tau/\tau_0)^4}$, with

$$\tau_0 \simeq \frac{1}{\sqrt{B}}\left[\sum_i \frac{\nu_i(\gamma_i A)^2}{4N}\frac{I_i(I_i+1)}{3}\right]^{-1/4}. \tag{2.8}$$

Surprisingly, when B is increased, τ_0 *decreases*. This behavior is opposite to the situation for electron spins, in which the echo decay time *increases* for increasing B [54]. This decrease is due to rapid fluctuations in h_z from nuclear spins precessing at frequencies $\sim \gamma_i B$. The Hahn echo can no longer refocus these dynamical fluctuations at finite B, although Eq. (2.7) does predict partial recurrences (dash-dotted line in Fig. 2.2) due to the finite number of discrete precession frequencies $\sim \gamma_i B$.

In contrast, at large magnetic field, $B \gtrsim A/(\gamma_i\sqrt{N})$, the system enters a motional-averaging regime in which the decay of $\langle S_x(2\tau)\rangle$ is bounded by $\sim (A/B\gamma_i\sqrt{N})^2$, giving rise to beating (black solid curve in Fig. 2.2). This beating has the same physical origin as electron-spin-echo envelope modulation (ESEEM) [55], although the extreme anisotropy of the hole hyperfine interaction allows uniquely for its complete suppression. Fig. 2–3 shows the $1/e$ decay time, τ_0, as B is increased, leading to a discontinuity when $\gamma_i B\sqrt{N}/A \gtrsim 1$, at which point $\langle S_x(2\tau)\rangle$ always remains close to its initial value [see Eq. (2.7)].

2.4 Finite $g_\perp$

Although there are definite advantages to making flat unstrained dots leading to $g_\perp \simeq 0$ and $h_{x,y} \simeq 0$, current experiments are performed on hole systems with finite (albeit small) $g_\perp$ [56, 2]. For this general case, with $\gamma_H = g_\perp \mu_B \neq 0$, we have no closed-form exact solution for the dynamics, but our analysis can still be applied for a certain range of τ, B.

We neglect subleading oscillating terms in the Magnus expansion when $\|(H^{(0)})^2\| \gg \|H^{(0)}H^{(2)}\|, \|\left(H^{(1)}\right)^2\|$. More specifically, if the relevant fast oscillation frequency is $\omega \sim \gamma_i B$, each precessing nuclear spin experiences a typical hyperfine field $\delta\omega_{\rm rms} \sim A/N$ from the hole. Otherwise, if the fast frequency is $\omega \sim \gamma_H B$, the hyperfine field acting on the precessing hole is of order $\delta\omega_{\rm rms} \sim A/\sqrt{N}$, averaging over the nuclear configurations. As a consequence, the parameter $\delta\omega_{\rm rms}/\omega < 1$ controls the expansion with $\delta\omega_{\rm rms}$ and ω given in Table 2–1 for each regime. In addition to bounded oscillating terms, the Magnus expansion generates terms that grow with τ. These terms approach ~ 1 at $\tau \sim \tau_{\rm max}$,

beyond which a finite-order Magnus expansion may fail. Nevertheless, the Magnus expansion will provide an accurate description whenever $\delta\omega_{\rm rms}/\omega < 1$ and for $\tau \lesssim \tau_{\rm max}$. Estimates of $\tau_{\rm max}$ are given in Table 2–1. The sufficient conditions presented here may be overly conservative in specific cases. For example, the parameters of the $B = 50$ mT curve of Fig. 2.2 give a short $\tau_{\rm max} < 0.1$ ns, while the Magnus expansion is clearly valid up to a much longer time scale. This is, however, a fortuitous example; we find that in analogous calculations of free-induction decay, the bounds are tight.

In practice, the value $g_\perp = 0.04$ measured in [56] suggests that $\gamma_H \gg \gamma_i$ in many current experiments. For $g_\perp = 0.04$, the condition $B > A/(\gamma_H\sqrt{N})$ is already satisfied above a rather small value, $B \gtrsim 100$ mT for $N \sim 10^4$. In Fig. 2–4 we plot representative curves in this motional-averaging regime, displaying the same features discussed for $g_\perp = 0$. Additionally, fast oscillations at the hole Zeeman frequency, $\gamma_H B$, induce beating in the echo envelope function, $\langle S_x(2\tau)\rangle$, which is not present for $g_\perp = 0$.

2.5 Decay anisotropy

While the results discussed so far are specific to π_x-pulses, other schemes are possible. Due to the extreme anisotropy of the hole-spin hyperfine coupling, the spin-echo decay is also highly anisotropic, depending on both the initialization and π-pulse axes. If the hole spin is initialized along a generic in-plane direction $\hat{n} = n_x\hat{x} + n_y\hat{y}$, and π-rotations are performed about that same axis, we find that $\langle \mathbf{S}(2\tau)\cdot\hat{n}\rangle/\langle \mathbf{S}(0)\cdot\hat{n}\rangle$ is independent of $\hat{n}$ when $g_\perp = 0$. This result is to be expected since any in-plane component of the hole spin experiences the same

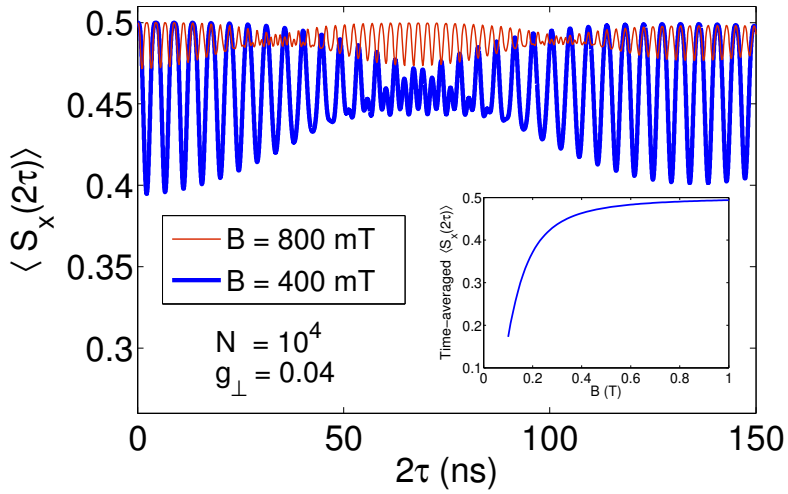

Figure 2–4: (Color online) Main panel: spin-echo envelope from a leading-order Magnus expansion when $\gamma_H \gg \gamma_i$ in the motional-averaging regime, $\gamma_H B > A/\sqrt{N}$. Inset: Time-averaged $\langle S_x(2\tau)\rangle$. We have taken $g_\perp = 0.04$ [56], $\langle S_x(0)\rangle = 1/2$, and $N = 10^4$. These results are valid at least for $2\tau \lesssim 2\tau_{\max} \simeq 70\,\text{ns}\,(140\,\text{ns})$ for $B = 400\,\text{mT}\,(B = 800\,\text{mT})$.

effective field, $\tilde{h}_z(t)$, along the z-axis. On the other hand, for $g_\perp \neq 0$, rotational symmetry about the z-axis is broken, resulting in a strong in-plane anisotropy. For the parameters of Fig. 2–4, but with initialization along $\hat{y}$ and π_x-pulses, we obtain that $\langle S_y(2\tau)\rangle$ is dominated by the hole Larmor precession about the x-axis and approaches the simple sinusoidal function $\langle S_y(2\tau)\rangle \simeq \langle S_y(0)\rangle \cos(2\gamma_H B\tau)$ in the motional-averaging regime, $\gamma_H B > A/\sqrt{N}$.

Additional dephasing mechanisms other than the nuclear bath can also have a strong influence on the precession about $\hat{x}$, introducing other sources of anisotropy. In particular, the decay of $\langle S_y(2\tau)\rangle$ was measured in [2] with π_z-pulses used for the Hahn echo. The resulting decay was found to be approximately exponential, $\langle S_y(2\tau)\rangle \simeq \langle S_y(0)\rangle e^{-2\tau/T_2}$, with a B-independent $T_2 \sim 1\,\mu$s. This behavior was

attributed to spectral diffusion induced by electric-field noise, which we model here by setting $\gamma_H B \rightarrow \gamma_H B + \delta\omega(t)$ in Eq. (2.1). The observed exponential decay is consistent with Gaussian white noise [57] $\langle \delta\omega(t)\delta\omega(t')\rangle_{\delta\omega} = \frac{2}{T_2}\delta(t-t')$ (and $\langle \delta\omega(t)\rangle_{\delta\omega} = 0$), where $\langle \ldots \rangle_{\delta\omega}$ indicates averaging with respect to realizations of $\delta\omega(t)$. We have included this additional dephasing mechanism in the evaluation of Eq. (2.6) for the π_x-pulse echo sequence examined previously and obtained a power-law decay at $\tau \gg T_2$:

$$\frac{\langle S_x(2\tau)\rangle}{\langle S_x(0)\rangle} \simeq \langle \exp\left[\frac{\langle h_z^2\rangle_I}{2}\sum_{\alpha=y,z} f_\alpha^2(t)\right]\rangle_{\delta\omega} \simeq \frac{1}{1+\tau/\tau_D}, \tag{2.9}$$

where $f_y(\tau) = \int_0^{2\tau} \sin\phi(t)\mathrm{sgn}(\tau - t)dt$, $f_z(\tau) = \int_0^{2\tau}\cos\phi(t)dt$, $\phi(t) = \gamma_H B t + \int_0^t \delta\omega(t')dt'$, and

$$\tau_D = \frac{1+(\gamma_H B T_2)^2}{2\langle h_z^2\rangle_I T_2}. \tag{2.10}$$

This decay time scale is exceedingly long ($\tau_D \simeq 20$ s) for the experimental value $\gamma_H B \simeq 2\times 10^{11}\,\mathrm{s}^{-1}$ and using $\langle h_z^2\rangle_I \sim 10^{15}\,\mathrm{s}^{-2}$, which demonstrates the negligible effect of spectral diffusion on the previous discussion (e.g., Figs. 2.2, 2–3, and 2–4). For simplicity, we have derived Eqs. (2.9) and (2.10) with static nuclear-field fluctuations $\langle h_z^2\rangle_I$. This corresponds to a worst-case scenario for the present model. At the high magnetic field of Ref. [2] ($B \sim 8$ T), motional averaging would likely inhibit decay even further.

2.6 Conclusion

We have calculated the spin-echo dynamics of a single heavy-hole spin in a flat unstrained quantum dot. The relevant dynamics are highly anisotropic in the spin components and π-rotation axes. When $\gamma_H \ll \gamma_i$, we predict an initial decrease

of the coherence time with increasing B, followed by a complete refocusing of the HH-spin signal and motional averaging when $B \gtrsim B_c$ ($B_c \sim A/\gamma_i\sqrt{N} \simeq 3\,\mathrm{T}$ for $N = 10^4$). The motional-averaging regime is also realized when $\gamma_H \gg \gamma_i$, relevant to current experiments. In this regime, decay due to the hyperfine coupling can only occur for $\tau \gtrsim \tau_{\max} \propto B$, and can therefore be completely suppressed. We have further shown that device-dependent electric-field noise becomes negligible for a specific geometry, allowing for a measurement of the limiting intrinsic decoherence due to nuclear spins. We expect the systematic approximation scheme introduced here to find wide applicability to a number of other challenging spin dynamics problems associated with nitrogen vacancy centers, donor impurities, and electrons in quantum dots.

Introduction to chapter 3

Chapter 2 focuses on spin-echo dynamics for the spin component along the external magnetic field to demonstrate how motional averaging in moderate applied fields can render the hyperfine interaction ineffective as a decoherence source. In this chapter, we examine the dynamics of all spin components and the consequences of anisotropy in the hyperfine coupling.

Section 3.1 establishes the form of the full Hamiltonian given the geometry of interest and discusses the conditions under which the Ising form of the heavy-hole hyperfine Hamiltonian is valid. Before presenting the general case with finite hole g-factor $g_\perp$, we consider the simpler $g_\perp \simeq 0$ case in section 3.2, where an exact solution can be found and is used to confirm the accuracy of the approximate solution derived in section 3.3. Calculations of the spin purity in section 3.3.1 reveal that this quantity is maximal when initializing along the hyperfine-induced fluctuations, perpendicular to the magnetic field. Since one could expect spin purity to be best-preserved for a hole spin prepared in a Zeeman eigenstate, this result calls for closer attention to geometry when carrying out experiments. Section 3.3.2 discusses in detail the sizes of higher-order terms and the regimes of validity for our approximation scheme based on the Magnus and moment expansions, and finally, section 3.4 compares the free-induction solution to a

previous calculation, which shows that the validity bounds we give in section 3.3.2 can be tight in some situations.

This chapter is a manuscript-in-progress to be submitted to Phys. Rev. B, and is therefore intended to be a self-contained article; any information from chapter 2 which is repeated here is necessary to provide context and a logical continuity.

CHAPTER 3
Maximizing heavy-hole spin purity

[X. J. Wang, Stefano Chesi, and W. A. Coish, in preparation.]

3.1 Model

We consider a heavy hole in a III-V semiconductor quantum dot grown along the [001] direction with negligible strain. The hyperfine interaction with surrounding nuclear spins is Ising-like in this case in the presence of a strong z-confinement potential, which generates a large splitting in zero-point energies, $\Delta_{\rm LH}$, between the heavy-hole ($J^z = \pm 3/2$) and light-hole ($J^z = \pm 1/2$) states.[12] We consider an in-plane magnetic field applied along the x-axis (see Fig. 3–1), resulting in the following Hamiltonian (setting $\hbar = 1$):

$$H = H_{\rm Z} + H_{\rm hf}, \tag{3.1}$$

$$H_{\rm Z} = -\gamma_H B S_x - \sum_k \gamma_{i_k} B I_k^x, \tag{3.2}$$

$$H_{\rm hf} = h_z S_z = \sum_k A_k I_k^z S_z. \tag{3.3}$$

Here, $H_{\rm Z}$ and $H_{\rm hf}$ are the Zeeman and hyperfine interactions, respectively. $\mathbf{S} = \boldsymbol{\sigma}/2$ is a pseudospin-1/2 operator in the heavy-hole subspace, $\boldsymbol{\sigma}$ is the vector of Pauli matrices, and $\mathbf{I}_k$ is the nuclear spin at site k. The hole gyromagnetic ratio is $\gamma_H = \mu_B g_\perp$, with μ_B the Bohr magneton and $g_\perp$ the in-plane hole g-factor. The gyromagnetic ratio of the $k^{\rm th}$ nucleus of isotopic species i_k having total

spin I_k is denoted by γ_{i_k}. The hyperfine coupling constants, A_k, are given by $A_k = A^{i_k} v_0 |\psi(\mathbf{r}_k)|^2$, where A^i is the hyperfine constant for nuclear species i, v_0 is the volume per nuclear spin, and $\psi(\mathbf{r}_k)$ is the heavy-hole envelope wavefunction evaluated at site $\mathbf{r}_k$. For a Gaussian envelope function in two dimensions,[11]

$$A_k \simeq (A/N) e^{-k/N}, \quad k = 0, 1, 2, ..., \tag{3.4}$$

where N is the number of nuclear spins within a quantum-dot Bohr radius.

Further assuming a uniform distribution of different nuclear species across the dot and $N \gg 1$ (typically $N \simeq 10^4 - 10^6$), we define the average hyperfine constant A as

$$A = \sum_k A_k \simeq \sum_i \nu_i A^i, \tag{3.5}$$

where ν_i is the isotopic abundance of species i. In our numerical estimates we will assume, for simplicity, a single average value A of the hyperfine constant where $A \simeq 13\mu$eV[12] for all nuclear species since A^i is of the same order for all isotopes of Ga, In, and As. For heavy holes, the ratio $|A/A^{(e)}|$ of hole to electron hyperfine coupling strengths has been estimated theoretically [12] in GaAs and confirmed experimentally [41, 42] in InGaAs and InP/GaInP to be $|A/A^{(e)}| \sim 0.1$.

Non-Ising corrections to the Hamiltonian have been shown to be small for unstrained, two-dimensional dots with pure heavy-hole states.[12] Hybridization with the light hole, conduction and split-off bands can lead to small non-Ising corrections on the order of $\sim$ 1% of A.[12] Higher-order transitions between the heavy-hole states via the light-hole subspace are also suppressed by at least $A/\Delta_{\mathrm{LH}} \ll 1$, where $\Delta_{\mathrm{LH}} \sim 100$ meV has been estimated [12] for a dot with

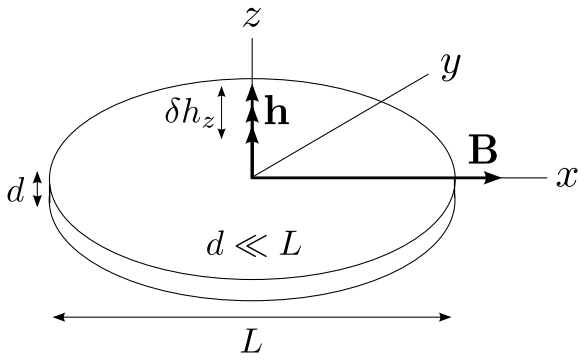

Figure 3–1: We assume the hole spin to be located in a flat unstrained quantum dot having thickness d much smaller than width L, subjected to a magnetic field $\mathbf{B}$ applied in-plane and a hyperfine-induced nuclear Overhauser field $\mathbf{h}$ fluctuating with amplitude δh_z.

thickness $d = 5$nm (see Fig. 3–1). Non-Ising corrections due to a finite dot thickness have been found theoretically to contribute to dynamics on a time scale $\gtrsim 10\,\mu$s,[38] much longer than the typical time scale we predict for hyperfine-induced hole-spin dephasing ($\lesssim 100$ns for the parameters used in Fig. 3–4 below).

Heavy-hole spins typically have a very small in-plane g-factor $|g_\perp| \ll 1$. The $g_\perp \to 0$ limit is approached for an unstrained quantum dot with strong confinement along the z-axis ([001] crystallographic direction),[12] a condition approximately realized in gated lateral quantum dots. The limit of weak strain also justifies neglecting the coupling of electric quadrupole moments of nuclear spins with $I > 1/2$ to electric field gradients. The typical size of the quadrupolar splitting E_Q has been estimated as[8] $E_Q \simeq 0.01\mu\text{eV} \simeq 10^{-3}A$ by considering the quadrupole moment of ^{69}Ga interacting with the field gradient due to the nonuniform charge density of the heavy hole. Finally, nuclear dipole-dipole interactions have been neglected in Eq. (3.1) as well. Dipole-dipole coupling will

influence the Hahn-echo decay of an electron spin on a timescale $\tau_{dd} \sim 10\,\mu$s $\propto 1/\sqrt{A^{(e)}}$.[35] Due to the smaller value of A for holes, we expect τ_{dd} to be longer than for electrons ($\gtrsim 10\,\mu$s),[34, 54, 58] which is much greater than the decay time scales considered here ($\lesssim$ 100ns in Fig. 3–4 below). Recent experiments suggest that heavy-hole hyperfine coupling constants have different signs for different elements.[39] One possible explanation for the sign difference is provided by a theory which accounts for d-orbital contributions and predicts non-negligible non-Ising flip-flop terms in the heavy-hole hyperfine Hamiltonian. The Ising form of the Hamiltonian is, however, consistent with a previous experiment [30] which has demonstrated very long hole spin-flip times at zero magnetic field.

Random fluctuations in the nuclear Overhauser field cause rapid hole-spin decoherence via the hyperfine coupling described previously. However, the process of spin echo can remove fluctuations which are approximately static over the time scale of hole-spin decay. To demonstrate the beneficial effect of a simple Hahn echo pulse sequence, we move into the interaction picture with respect to the Zeeman terms $H_{\rm Z}$, transforming the Hamiltonian to

$$\tilde{H}_{\rm hf}(t) = e^{iH_{\rm Z}t} H_{\rm hf} e^{-iH_{\rm Z}t} = \tilde{h}_z(t)\tilde{S}_z(t), \tag{3.6}$$

where, for any operator $\mathcal{O}$,

$$\tilde{\mathcal{O}}(t) = e^{iH_{\rm Z}t}\mathcal{O}e^{-iH_{\rm Z}t}. \tag{3.7}$$

In particular, $\tilde{h}_z(t)$ and $\tilde{S}_z(t)$ are explicitly given by:

$$\tilde{h}_z(t) = \sum_k A_k[I_k^z \cos(\gamma_{i_k} Bt) - I_k^y \sin(\gamma_{i_k} Bt)], \tag{3.8}$$

$$\tilde{S}_z(t) = [S_z \cos(\gamma_H Bt) - S_y \sin(\gamma_H Bt)]. \tag{3.9}$$

Accounting for π-pulses at times $t = \tau$ and $t = 2\tau$ about an axis α, where $\alpha = x, y, z$, the echo Hamiltonian $\tilde{H}_e(t)$ becomes piecewise defined:

$$\tilde{H}_e(t) = \begin{cases} \tilde{H}(t) & 0 \leq t < \tau, \\ \sigma_\alpha \tilde{H}(t) \sigma_\alpha & \tau \leq t \leq 2\tau. \end{cases} \tag{3.10}$$

The final π-pulse at $t = 2\tau$ returns the spin to its initial orientation. From Eqs. (3.6)-(3.9), when $\alpha = x$, the Hamiltonian simply acquires a factor of -1 between $t = \tau$ and $t = 2\tau$ from the echo pulse sequence. If $\tilde{H}(t) \simeq \tilde{H}(0)$ were further assumed to be constant, the π-pulse at $t = \tau$ would reverse the time evolution and refocus the hole spin at $t = 2\tau$. This process is illustrated in Fig. 3–2(a), where dephasing due to slowly-varying hyperfine-induced fluctuations about $\hat{\mathbf{z}}$ is removed by the echo. Since π-pulses about $\hat{\mathbf{y}}$ or $\hat{\mathbf{z}}$ do not reverse the sign of the Hamiltonian from $t = \tau$ to $t = 2\tau$, in this work we will focus on π-rotations about $\hat{\mathbf{x}}$ when discussing decoherence due to the hyperfine interaction.

In recent experiments, other dephasing mechanisms may have had larger effects than coupling to the nuclear bath. In particular, the authors of Ref. [2] attribute their spin-echo coherence time T_2 to electric-field-induced charge noise, which introduces fluctuations in the frequency of hole-spin precession about the applied magnetic field along $\hat{\mathbf{x}}$. The spin-echo sequence implemented in Ref. [2]

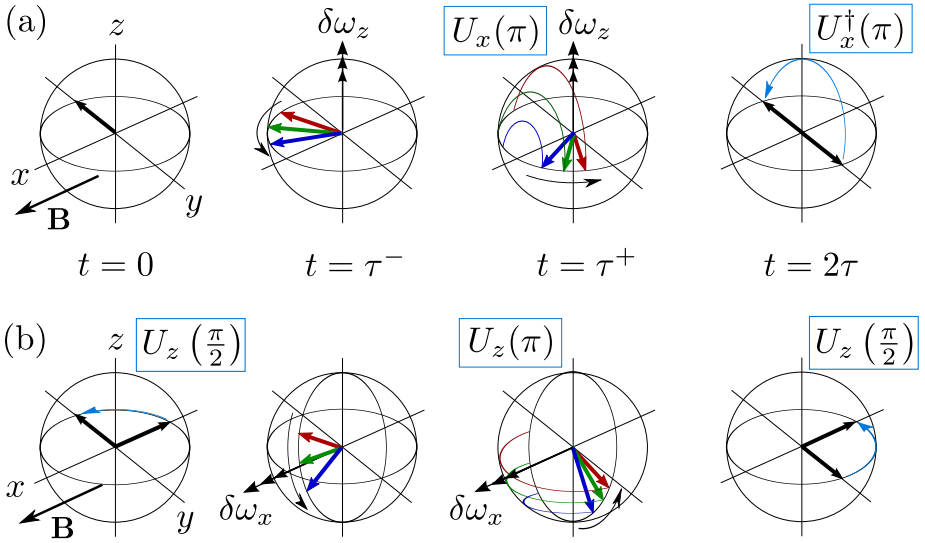

Figure 3–2: (Color online) (a) Echo sequence with π-rotations about $\hat{\mathbf{x}}$, which reverses dephasing from static fluctuations $\delta\omega_z$ along $\hat{\mathbf{z}}$ due to the hyperfine interaction. For the sake of clarity we have assumed $g_\perp \simeq 0$ such that there is no precession of the hole spin about $\hat{\mathbf{x}}$. (b) Echo sequence with rotations about $\hat{\mathbf{z}}$, which reverses dephasing from static fluctuations $\delta\omega_x$ along $\hat{\mathbf{x}}$ due to electric-field fluctuations.

therefore eliminates dephasing due to static fluctuations along $\hat{\mathbf{x}}$ and is shown in Fig. 3–2(b). A phenomenological theory has been developed in chapter 2 to show that dephasing due to electric-field-induced fluctuations can be suppressed in the geometry of Fig. 3–2(a), but further investigation is needed to fully understand this decoherence mechanism.

3.2 Exact spin-echo dynamics ($g_\perp = 0$)

We first consider the ideal two-dimensional limit ($d \ll L$, with L the typical quantum-dot width, shown in Fig. 3–1), where we take $g_\perp \cong 0$ and the

Hamiltonian reduces to:

$$H = h_z S_z + \sum_k B\gamma_k I_k^x. \tag{3.11}$$

We find an exact solution for evolution under the Hamiltonian of Eq.(3.11) which will be accurate whenever $|\gamma_H| \ll |\gamma_i|$, or equivalently, $|g_\perp| \lesssim 10^{-3}$ if we take $|\gamma_i| \sim 5 \times 10^7 \mathrm{radT}^{-1}\mathrm{s}^{-1}$ for all isotopes of In, Ga, and As. This limit should be achievable since $|g_\perp| < 5 \times 10^{-3}$ has been reported in 2D AlGaAs wells.[52] A systematic approximation scheme (valid for $g_\perp \neq 0$) will be developed in the following sections. The exact solution presented here will allow us to confirm the validity of our approximation scheme in the limit $g_\perp \to 0$.

As seen in Eqs.(3.12) and (3.13) below, Eq. (3.11) is block diagonal in the eigenbasis of S_z:

$$\langle \Uparrow | \; H \; | \Uparrow \rangle = \sum_k \left(B\gamma_k I_k^x + \frac{1}{2} A_k I_k^z \right) = \sum_k \mathbf{h}_k^{\uparrow} \cdot \mathbf{I}_k, \tag{3.12}$$

$$\langle \Downarrow | \; H \; | \Downarrow \rangle = \sum_k \left(B\gamma_k I_k^x - \frac{1}{2} A_k I_k^z \right) = \sum_k \mathbf{h}_k^{\downarrow} \cdot \mathbf{I}_k. \tag{3.13}$$

The eigenstates of $\mathbf{h}_k^{\uparrow} \cdot \mathbf{I_k}$ and $\mathbf{h}_k^{\downarrow} \cdot \mathbf{I}_k$ are obtained after rotating I_k^z-eigenstates about $\hat{\mathbf{y}}$ by an angle θ_k and $\pi - \theta_k$, respectively, with θ_k shown in Fig. 3–3 and given by

$$\theta_k = \arctan \frac{2B\gamma_k}{A_k}. \tag{3.14}$$

The in-plane expectation value of the hole spin is $\langle \mathbf{S}(2\tau) \rangle \cdot \hat{n}_\perp$, where $\hat{n}_\perp = (n_x, n_y)$ is a unit vector, and for any operator $\mathcal{O}$, the brackets $\langle \mathcal{O} \rangle = \mathrm{Tr}\{\mathcal{O}\rho\}$ denote the expectation value taken with respect to an initial state ρ. We assume an initial state $\rho = \rho_S \otimes \rho_I$, which is a tensor product of the hole-spin (ρ_S)

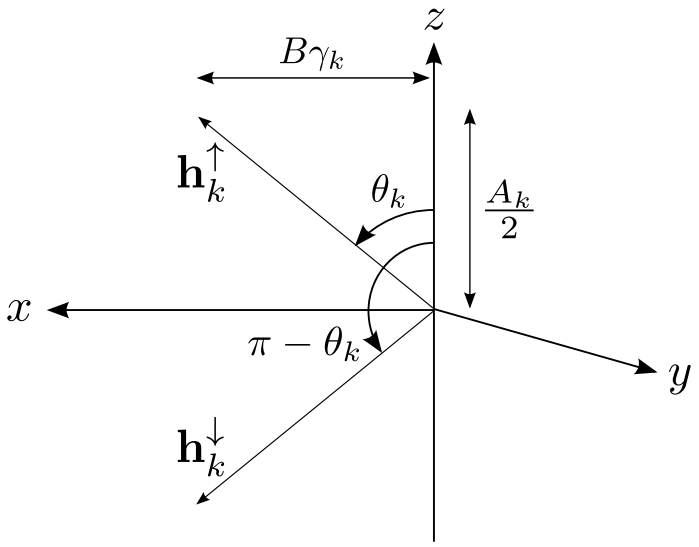

Figure 3–3: Effective fields $\mathbf{h}_k^{\uparrow}$ ($\mathbf{h}_k^{\downarrow}$) at the position of the k^{th} nuclear spin, with hole spin up (down), expressed in terms of the hyperfine coupling A_k and Zeeman energy $\gamma_k B$ of the nuclear spin at site k.

and nuclear-spin (ρ_I) density matrices, and the nuclear-spin density matrix $\rho_I = \bigotimes_{k=1}^{N} \rho_k$ is further assumed to factorize into the density matrices of individual nuclear spins ρ_k. Since the Hamiltonian in the $g_\perp = 0$ limit [Eq.(3.11)] is invariant under rotations of the hole spin $\mathbf{S}$ about $\hat{\mathbf{z}}$, $\langle \mathbf{S}(2\tau)\rangle \cdot \hat{n}_\perp$ is similarly invariant under z-rotations, and is therefore given generally in terms of the x-component:

$$\langle S_x(2\tau)\rangle / \langle S_x(0)\rangle = \tag{3.15}$$
$$\mathrm{Re} \prod_{k=1}^{N} \mathrm{Tr}\left\{ \left(E_k R_k E_k R_k^{-1} E_k^{-1} R_k E_k^{-1} R_k^{-1} \right) \rho_k \right\},$$

where $E_k = E_k(2\tau)$ (the explicit time dependence was dropped in Eq.(3.15) for notational brevity) represents the time evolution operator acting on the k^{th} nuclear

spin eigenstate, having matrix elements

$$\langle I_k, m \mid E_k(2\tau) \mid I_k, m' \rangle = e^{i|\mathbf{h_k}|(I_k - m + 1)\tau} \delta_{m,m'}, \tag{3.16}$$

where $|\mathbf{h_k}| = |\mathbf{h}_k^{\uparrow}| = |\mathbf{h}_k^{\downarrow}|$ is the magnitude of the effective fields $\mathbf{h}_k^{\uparrow}$ and $\mathbf{h}_k^{\downarrow}$, and finally, $R_k = R^y(\pi - 2\theta_k)$ is a rotation about the y-axis by an angle $(\pi - 2\theta_k)$.

The nuclear-spin bath is taken to be in an infinite-temperature thermal state. To simulate this state numerically from a smaller sample, we take

$$\rho_k = \frac{1}{N_i} \sum_{j=1}^{N_i} \left| \psi_{I_k}^j(0) \right\rangle \left\langle \psi_{I_k}^j(0) \right|, \tag{3.17}$$

$$\left| \psi_{I_k}^j(0) \right\rangle = R^z(\phi_k^j) R^y(\theta_k^j) \left| I_k, m_k^j \right\rangle, \tag{3.18}$$

where N_i is the number of different initial nuclear-spin configurations to average over, the polar angle θ_k^j is randomly chosen between 0 and π (with probability $\propto \sin\theta_k^j$), ϕ_k^j is the randomly chosen azimuthal angle between 0 and 2π, and finally m_k^j is sampled uniformly from the set of values $m_k^j = \{-I_k, -I_k + 1, \cdots, I_k - 1, I_k\}$. Given the large number of nuclear spins N, only a small number of initial configurations ($N_i \simeq 10$) is needed before convergence, which is sensible since the number of possible nuclear-spin states grows exponentially with N_i. In Fig. 3–4, we used $N_i = 10$.

The hole-spin-echo dynamics of Eq.(3.15) is plotted in Fig. 3–4 for several values of the applied magnetic field. As the magnetic field is increased from $B = 0$, the decay time initially decreases until the system crosses over into a motional-averaging regime where the decay becomes bounded and coherence is then preserved.[1] This nontrivial dependence on the magnetic field can be more

readily understood by studying the approximate solution, from which an intuitive physical picture will emerge.

3.3 Spin-echo dynamics

To solve the more general problem with $g_\perp \neq 0$, we build an approximation scheme based on the Magnus expansion, an average-Hamiltonian theory applicable to systems undergoing rapid periodic oscillations.[53] Such rapid oscillations are present in the interaction-picture Hamiltonian of Eq.(3.6) for sufficiently large B. Using the Magnus expansion, we rewrite the time-evolution operator $\tilde{U}(2\tau)$ in terms of a series expansion,

$$\tilde{U}(2\tau) = \mathcal{T} e^{-i\int_0^{2\tau} dt \tilde{H}_e(t)} = e^{-iH_M(2\tau)}, \tag{3.19}$$

$$H_M(2\tau) = \sum_{i=0}^{\infty} H^{(i)}(2\tau), \tag{3.20}$$

where $\mathcal{T}$ is the usual time-ordering operator and all terms in $H_M(2\tau)$ can be obtained through the Baker-Campbell-Hausdorff formula. The leading-order term is $H^{(0)}(2\tau) = \overline{H(2\tau)}2\tau$, where $\overline{H(2\tau)}$ is simply the average of $\tilde{H}_e(t)$ over a time interval 2τ. Each higher-order term contains an additional factor of A_k as well as one more integral over time, resulting in oscillating terms which are typically suppressed by a factor of A_k/ω, with $\omega \cong \gamma_i B$ (if $\gamma_H \ll \gamma_i$) or $\omega \cong \gamma_H B$ (if $\gamma_H \gg \gamma_i$).

The time-evolved spin components S_α ($\alpha = x, y, z$) are given by

$$\langle S_\alpha(2\tau)\rangle = \left\langle \tilde{U}^\dagger(2\tau)\tilde{S}_\alpha(2\tau)\tilde{U}(2\tau)\right\rangle. \tag{3.21}$$

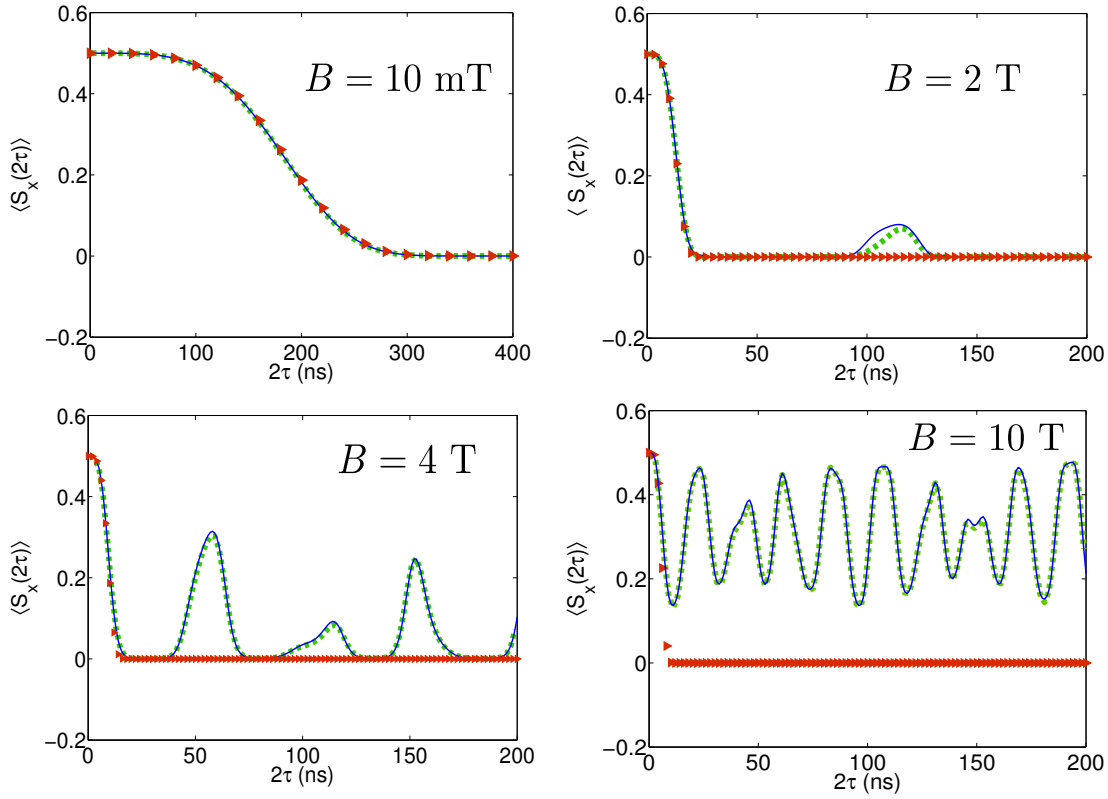

Figure 3–4: (Color online) Exact [Eq.(3.15), solid lines], approximate [Eq.(3.38), dotted lines], and short-time [Eq.(3.39), triangles] solutions for a range of magnetic fields B. We have assumed an $In_xGa_{1-x}As$ material with $x = 0.5$, $\langle S_x(0)\rangle = 1/2, N = 10^4, N_i = 10, \gamma_H = g_\perp \mu_B = 0$, and values for γ_i and I_i were obtained from Ref. [8].

Defining the Liouvillian $L_{\mathrm{M}}(2\tau)$,

$$L_{\mathrm{M}}(2\tau)\mathcal{O} = [H_{\mathrm{M}}(2\tau), \mathcal{O}]\,, \tag{3.22}$$

we rewrite $\langle S_\alpha(2\tau)\rangle$ as

$$\langle S_\alpha(2\tau)\rangle = \left\langle \left[e^{iL_M(2\tau)} \tilde{S}_\alpha(2\tau) \right] \right\rangle . \tag{3.23}$$

We again take the initial state $\rho = \rho_S \otimes \rho_I$ as a tensor product of the hole-spin and nuclear-spin density matrices. Assuming an infinite-temperature nuclear spin state with $N \gg 1$ uncorrelated nuclear spins, we apply a Gaussian approximation scheme[59] based on the central-limit theorem (see Appendix A for details):

$$\begin{aligned} &\left\langle \left[e^{iL_{\mathrm{M}}(2\tau)} \tilde{S}_\alpha(2\tau) \right] \right\rangle \simeq \\ &\left\langle \left\{ \exp\left[-\frac{1}{2} \left\langle L_{\mathrm{M}}^2(2\tau) \right\rangle_I \right] \tilde{S}_\alpha(2\tau) \right\} \right\rangle_S , \end{aligned} \tag{3.24}$$

where we specify that for any operator $\mathcal{O}_S$ acting in the hole-spin space,

$$\langle L_{\mathrm{M}}^2(2\tau)\rangle_I \mathcal{O}_S = \mathrm{Tr}_I \left\{ \left[L_{\mathrm{M}}^2(2\tau)\mathcal{O}_S \right] \rho_I \right\}, \tag{3.25}$$

$$\langle \mathcal{O}_S \rangle_S = \mathrm{Tr}_S\{\mathcal{O}_S \rho_S\}. \tag{3.26}$$

In what follows, we will assume a magnetic field large enough to justify keeping only the leading-order term in the Magnus expansion, so that $H_{\mathrm{M}}(2\tau) \cong H^{(0)}(2\tau)$. To simplify the notation, we redefine the leading-order nuclear-spin-averaged Liouvillian as

$$\mathcal{L}(2\tau) = \left\langle \left[L^{(0)}(2\tau) \right]^2 \right\rangle_I , \tag{3.27}$$

where $L^{(0)}(2\tau)\mathcal{O} = \left[H^{(0)}(2\tau), \mathcal{O}\right]$. Combining Eqs.(3.23), (3.24), and (3.27) allows us to rewrite the evolution of an arbitrary spin component as

$$\langle S_\alpha(2\tau)\rangle \simeq \left\langle \left[e^{-\frac{1}{2}\mathcal{L}(2\tau)}\tilde{S}_\alpha(2\tau)\right]\right\rangle_S . \tag{3.28}$$

Precise conditions justifying the validity of the leading-order Magnus expansion will be given in section 3.3.2.

In the $\{S_x, S_y, S_z\}$ basis, the matrix elements $[\mathcal{L}(2\tau)]_{\alpha\beta}$ of the leading-order Liouvillian are defined by

$$\mathcal{L}(2\tau)S_\alpha = \sum_\beta [\mathcal{L}(2\tau)]_{\beta\alpha} S_\beta; \quad \alpha, \beta = x, y, z, \tag{3.29}$$

where the matrix representation $[\mathcal{L}(2\tau)]$ is given by

$$[\mathcal{L}(2\tau)] = \begin{pmatrix} h^{yy}(2\tau) + h^{zz}(2\tau) & 0 & 0 \\ 0 & h^{zz}(2\tau) & -h^{yz}(2\tau) \\ 0 & -h^{yz}(2\tau) & h^{yy}(2\tau) \end{pmatrix}. \tag{3.30}$$

Here, $h^{\gamma\delta}(2\tau), \gamma, \delta = y, z$ are defined by

$$h^{\gamma\delta}(2\tau) = \sum_{k,\alpha=y,z} A_k^2 g_k^{\alpha\gamma}(2\tau) g_k^{\alpha\delta}(2\tau) \frac{I_k(I_k+1)}{3}, \tag{3.31}$$

$$H^{(0)}(2\tau) = \sum_{\substack{k,\alpha=y,z \\ \beta=y,z}} A_k g_k^{\alpha,\beta}(2\tau) I_k^\alpha S^\beta, \tag{3.32}$$

where $g_k^{\alpha,\beta}(2\tau)$ are rapidly oscillating terms having amplitudes proportional to $1/\omega$, with $\omega = B \cdot \max\{\gamma_i, \gamma_H\}$ the fast oscillation frequency. Explicit expressions for $g_k^{\alpha,\beta}(2\tau)$ are given in Eqs.(B.5)-(B.8) of Appendix B. Diagonalizing the above

Eigenvectors
$\hat{\mathbf{e}}_x = \hat{\mathbf{x}}$
$\hat{\mathbf{e}}_+(2\tau) = \cos\theta(2\tau)\hat{\mathbf{y}} + \sin\theta(2\tau)\hat{\mathbf{z}}$
$\hat{\mathbf{e}}_-(2\tau) = -\sin\theta(2\tau)\hat{\mathbf{y}} + \cos\theta(2\tau)\hat{\mathbf{z}}$

Eigenvalues
$\lambda_x(2\tau) = 2\bar{h}(2\tau)$
$\lambda_\pm(2\tau) = \bar{h}(2\tau) \pm \sqrt{\delta h^2(2\tau) + (h^{yz}(2\tau))^2}$

Table 3–1: Eigenvectors $\hat{\mathbf{e}}_\mu(2\tau)$, $\mu = x, \pm$, and eigenvalues $\lambda_\mu(2\tau)$ which satisfy Eq.(3.33), the eigenvalue equation for the leading-order Liouvillian $\mathcal{L}(2\tau)$. $\theta(2\tau)$, $\bar{h}(2\tau)$, and $\delta h(2\tau)$ are defined in Eqs.(3.34)-(3.36).

matrix, we define the hole-spin eigenoperators $\mathbf{S}\cdot\hat{\mathbf{e}}_\mu(2\tau)$ and their associated eigenvalues $\lambda_\mu(2\tau)$ by the following equation:

$$\mathcal{L}(2\tau)\mathbf{S}\cdot\hat{\mathbf{e}}_\mu(2\tau) = \lambda_\mu(2\tau)\mathbf{S}\cdot\hat{\mathbf{e}}_\mu(2\tau), \tag{3.33}$$

where $\mu = x, \pm$ and the eigenvector $\hat{\mathbf{e}}_\mu(2\tau)$ is a generally time-dependent unit vector. Fig. 3–5 illustrates the eigenvectors, which are given along with their associated eigenvalues in table 3–1, with $\bar{h}(2\tau)$ and $\delta h(2\tau)$ defined as

$$\bar{h}(2\tau) = \frac{1}{2}\left[h^{yy}(2\tau) + h^{zz}(2\tau)\right] \tag{3.34}$$

$$\delta h(2\tau) = \frac{1}{2}\left[h^{zz}(2\tau) - h^{yy}(2\tau)\right]. \tag{3.35}$$

$\theta(2\tau)$ is the angle illustrated in Fig. 3–5 and given by

$$\theta(2\tau) = \frac{1}{2}\arctan\frac{-h^{yz}(2\tau)}{\delta h(2\tau)}. \tag{3.36}$$

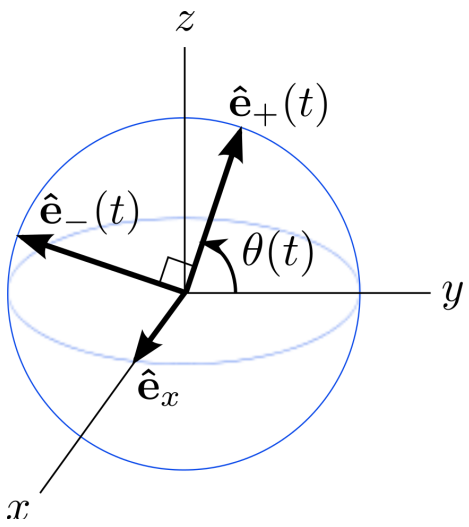

Figure 3–5: Unit eigenvectors of the leading-order Liouvillian $\mathcal{L}(2\tau)$, which form an orthonormal basis. $\hat{\mathbf{e}}_x$ is simply $\hat{\mathbf{x}}$ while $\hat{\mathbf{e}}_+(2\tau)$ and $\hat{\mathbf{e}}_-(2\tau)$ correspond to $\hat{\mathbf{y}}$ and $\hat{\mathbf{z}}$ rotated by an angle $\theta(2\tau)$ [given by Eq.(3.36)] about the x-axis.

The hole-spin evolution is therefore highly anisotropic and can be divided into two independent subspaces, since the Liouvillian does not mix the x-component of spin with the y- and z-components.

We will first discuss the behaviour in the S_x-subspace, where the spin-echo dynamics are given by

$$\frac{\langle S_x(2\tau)\rangle}{\langle S_x(0)\rangle} \simeq e^{-\frac{1}{2}\lambda_x(2\tau)} = e^{-\bar{h}(2\tau)} \tag{3.37}$$

Further setting $g_\perp = 0$ in the expressions for $h^{yy}(2\tau)$ and $h^{zz}(2\tau)$, Eq.(3.37) simplifies to

$$\frac{\langle S_x(2\tau)\rangle}{\langle S_x(0)\rangle} \simeq \exp\left[-\sum_i \frac{4\nu_i (A^i)^2 I_i(I_i+1)}{3N(\gamma_i B)^2} \sin^4\left(\frac{\gamma_i B\tau}{2}\right)\right]. \tag{3.38}$$

We compare the above expression directly with the exact solution in Fig. 3–4. A closer look at Eq.(3.38) reveals a simple explanation for the dependence of $\langle S_x(2\tau)\rangle$. For $B \ll A/(\gamma_i\sqrt{N})$ (top-left panel in Fig. 3–4), a short-time expansion of Eq.(3.38) yields

$$\begin{aligned}\langle S_x(2\tau)\rangle &\simeq \langle S_x(0)\rangle \left(1 - \left(\frac{2\tau}{\tau_0}\right)^4\right) \\ &\simeq \langle S_x(0)\rangle e^{-(2\tau/\tau_0)^4}, \qquad (3.39)\end{aligned}$$

$$\tau_0 \simeq \frac{1}{\sqrt{B}}\left[\sum_i \frac{\nu_i(\gamma_i A^i)^2}{4N}\frac{I_i(I_i+1)}{3}\right]^{-1/4}, \qquad (3.40)$$

where the initial decay time $\tau_0 \propto 1/\sqrt{B}$ decreases with increasing B. This behaviour is contrary to that of single electron spins, for which the spin-echo decay time always grows with increasing B.[54] In the case of hole spins, the precession of nuclear spins due to the in-plane magnetic field introduces dynamic fluctuations in h_z, resulting in decoherence which is not reversed by the spin echo. The nuclear Zeeman frequencies are proportional to B, hence an increase in B leads to faster fluctuations in h_z and shorter coherence times.

At larger magnetic fields, when $B \gg A/(\gamma_i\sqrt{N})$, however, decay in the hole-spin echo envelope is bounded and the amplitude of oscillations in $\langle S_x(2\tau)\rangle$ decreases with increasing B, as can be seen in Eq.(3.38) and in Fig. 3–4. In this regime, the nuclear Larmor precession is rapid enough to effectively average out fluctuations in h_z, a phenomenon known as motional averaging.

The y- and z- components of the hole-spin evolution can be calculated by inverting the equations for $\hat{\mathbf{e}}_+(2\tau)$ and $\hat{\mathbf{e}}_-(2\tau)$ from table 3–1,

$$S_y = \mathbf{S}\cdot\hat{\mathbf{y}} = \cos\theta(2\tau)\mathbf{S}\cdot\hat{\mathbf{e}}_+(2\tau) - \sin\theta(2\tau)\mathbf{S}\cdot\hat{\mathbf{e}}_-(2\tau), \tag{3.41}$$

$$S_z = \mathbf{S}\cdot\hat{\mathbf{z}} = \sin\theta(2\tau)\mathbf{S}\cdot\hat{\mathbf{e}}_+(2\tau) + \cos\theta(2\tau)\mathbf{S}\cdot\hat{\mathbf{e}}_-(2\tau), \tag{3.42}$$

and by defining the ladder operators $S'_\pm$:

$$S'_\pm = S_y \pm iS_z. \tag{3.43}$$

The expectation values of the hole spin components along y and z are then given by

$$\langle S_y(2\tau)\rangle = \mathrm{Re}\langle S'_+(2\tau)\rangle, \tag{3.44}$$

$$\langle S_z(2\tau)\rangle = \mathrm{Im}\langle S'_+(2\tau)\rangle, \tag{3.45}$$

with

$$\langle S'_+(2\tau)\rangle = e^{i\omega(2\tau)}\sum_{\mu=\pm}\sqrt{\mu}e^{-\frac{1}{2}\lambda_\mu(2\tau)\langle\mathbf{S}\rangle_0\cdot\hat{\mathbf{e}}_\mu(2\tau)}, \tag{3.46}$$

where $\omega(2\tau) = 2\gamma_H B\tau + \theta(2\tau)$, $\sqrt{+} = \sqrt{1} = 1$, and $\sqrt{-} = \sqrt{-1} = i$.

3.3.1 Maximizing Spin Purity

To quantify the irreversible loss of information due to entanglement between a central spin and its environment, it is useful to consider the spin purity, $P(2\tau)$, defined as [60]

$$P(2\tau) = \mathrm{Tr}\left[\rho_S^2(2\tau)\right] = \frac{1}{2} + 2|\langle\mathbf{S}(2\tau)\rangle|^2, \tag{3.47}$$

where $\rho_S(2\tau) = \frac{1}{2}I_2 + \langle \mathbf{S}(2\tau)\rangle \cdot \boldsymbol{\sigma}$ is the time-evolved final reduced density matrix for the hole-spin system. The purity determines how close the reduced density matrix is to a pure state; $P = 1$ if $\rho_S(2\tau)$ is a pure state and $P < 1$ for a mixed state. Maximizing the spin purity is equivalent to minimizing the information (or spin polarization) lost from mixing with the nuclear bath system, and is particularly important for purification protocols involving ancilla qubits.[61]

In the motional-averaging regime, the spin purity can be maximized by simply choosing to address the hole spin at specific times τ at which $|\langle \mathbf{S}(2\tau)\rangle|$ is maximal. In addition to choosing appropriate times, the initialization axis also affects the purity, since the Liouvillian $\mathcal{L}(2\tau)$ does not preserve the magnitude of all eigenvectors $\hat{\mathbf{e}}_\mu(2\tau),\ \mu = x, \pm$, equally. The orthonormality of the eigenvectors allows us to write the initial magnitude of the hole spin $|\langle \mathbf{S}\rangle_0|$ as

$$|\langle \mathbf{S}\rangle_0|^2 = \sum_{\mu=x,\pm} \left[\langle \mathbf{S}\rangle_0 \cdot \hat{\mathbf{e}}_\mu(2\tau)\right]^2 = \frac{1}{4}, \tag{3.48}$$

where $\langle \mathbf{S}\rangle_0 = \langle \mathbf{S}(0)\rangle$ is the initial expectation value of the hole spin. We can also express the magnitude of the time-evolved hole spin in terms of its components along $\hat{\mathbf{e}}_\mu(2\tau)$:

$$|\langle \mathbf{S}(2\tau)\rangle|^2 = \sum_{\mu=x,\pm} e^{-\lambda_\mu(2\tau)} \left[\langle \mathbf{S}\rangle_0 \cdot \hat{\mathbf{e}}_\mu(2\tau)\right]^2. \tag{3.49}$$

Furthermore, one can show that

$$\lambda_x(2\tau) \geq \lambda_+(2\tau) \geq \lambda_-(2\tau) \tag{3.50}$$

by rewriting $\lambda_{\pm}(2\tau)$ as

$$\lambda_{\pm}(2\tau) = \bar{h}(2\tau) \pm \sqrt{\bar{h}^2(2\tau) - \det\left([\mathcal{L}^{yz}(2\tau)]\right)} \tag{3.51}$$

and recognizing that $\det\left([\mathcal{L}^{yz}(2\tau)]\right) = \lambda_+(2\tau)\lambda_-(2\tau) \geq 0$ since the eigenvalues of the Liouvillian must be real and positive to ensure unitary evolution with probabilities bounded by 1. It follows that the inequality in Eq.(3.50) must hold for all time τ.

Combining Eqs.(3.48) and (3.49), we obtain

$$|\langle \mathbf{S}(2\tau)\rangle|^2 = \frac{1}{4}e^{-\lambda_-(2\tau)} + \sum_{\mu=x,+}\left(e^{-\lambda_\mu(2\tau)} - e^{-\lambda_-(2\tau)}\right)\left[\langle \mathbf{S}\rangle_0 \cdot \hat{\mathbf{e}}_\mu(2\tau)\right]^2.$$

Since $[e^{-\lambda_\mu(2\tau)} - e^{-\lambda_-(2\tau)}] \leq 0$ for $\mu = x/+$, $|\langle \mathbf{S}(2\tau)\rangle|^2$ is maximized when $|\langle \mathbf{S}\rangle_0 \cdot \hat{\mathbf{e}}_\mu(2\tau)| = 0$. The spin purity at time 2τ is therefore highest when initializing along the instantaneous orientation of $\hat{\mathbf{e}}_-(2\tau)$, yielding a maximal spin purity of

$$P_{\max}(2\tau) = \frac{1}{2}\left(1 + e^{-\lambda_-(2\tau)}\right), \quad |\langle \mathbf{S}\rangle_0 \cdot \hat{\mathbf{e}}_-(2\tau)| = \frac{1}{2}. \tag{3.52}$$

By the same argument, the minimal spin purity is achieved for initialization along $\hat{\mathbf{e}}_x(2\tau)$:

$$P_{\min}(2\tau) = \frac{1}{2}\left(1 + e^{-\lambda_x(2\tau)}\right), \quad |\langle \mathbf{S}\rangle_0 \cdot \hat{\mathbf{e}}_x(2\tau)| = \frac{1}{2}. \tag{3.53}$$

Initializing along any other axis results in a non-optimal purity, as illustrated by the black dotted curve in Fig. 3–6 corresponding to initialization along $\hat{\mathbf{e}}_+(2\tau)$. In this case, $P(2\tau)$ is given by

$$P_+(2\tau) = \frac{1}{2}\left(1 + e^{-\lambda_+(2\tau)}\right). \tag{3.54}$$

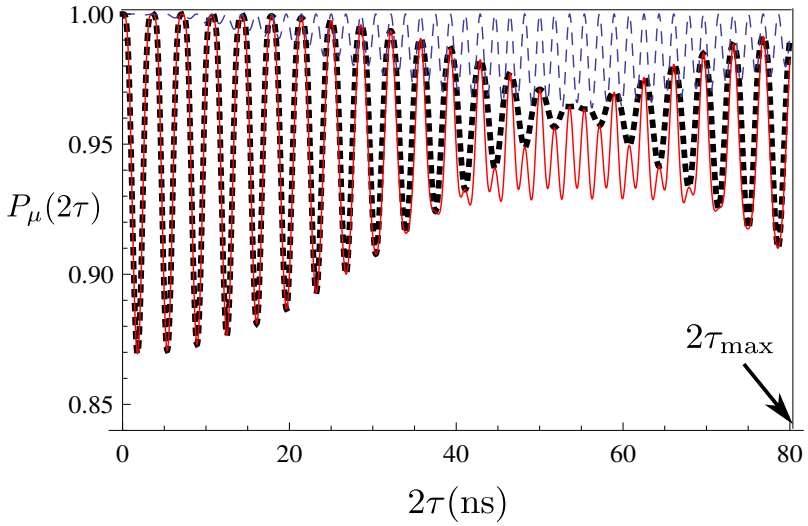

Figure 3–6: (Color online) Spin-echo purity $P(2\tau)$ for initialization along $\hat{\mathbf{e}}_-(2\tau)$ [Eq.(3.52), blue dashed line], $\hat{\mathbf{e}}_+(2\tau)$ [Eq.(3.54), black dotted line], and $\hat{\mathbf{e}}_x(2\tau)$ [Eq.(3.53), red solid line], with $B = 500$ mT, $g_\perp = 0.04$, $N = 10^4$, and γ_i and I_i from Ref. [8]. As will be discussed in section 3.3.2, the Magnus expansion is valid for $t < \tau_{\max}$, where $\tau_{\max} \sim B\gamma_H N/A^2$ for the parameters used in this plot (see table 3–2). The purity at time 2τ is maximized when initializing along $\hat{\mathbf{e}}_-(2\tau)$.

The blue dashed and red solid curves in Fig. 3–6 give $P_{\max}(2\tau)$ and $P_{\min}(2\tau)$, respectively.

3.3.2 Validity of Magnus expansion

Each subleading term in the Magnus expansion consists of a bounded oscillating part and an unbounded component whose amplitude increases with τ [see Eqs.(C.7)-(C.9) in Appendix C]. The bounded contributions of the lowest subleading terms in the Liouvillian $\langle L_M^2(2\tau)\rangle_I$ can be neglected if their amplitudes are small compared to the amplitude of the leading-order term. Explicitly, the

leading-order Liouvillian will dominate over subleading terms when

$$\frac{A}{NB\gamma_i} \ll 1 \qquad \text{if } \gamma_i \gg \gamma_H, \tag{3.55}$$

$$\frac{A}{\sqrt{N}B\gamma_H} \ll 1 \qquad \text{if } \gamma_H \gg \gamma_i. \tag{3.56}$$

These conditions imply that the expansion is valid over a greater range of B for the $\gamma_i \gg \gamma_H$ case than for the $\gamma_H \gg \gamma_i$ case. In fact, if $\gamma_H \gg \gamma_i$, the Magnus expansion is strictly valid only in the motional averaging regime, which is defined as

$$B \gtrsim \frac{A}{\sqrt{N}\gamma_{\max}}, \quad \gamma_{\max} = \max\{\gamma_H, \gamma_i\}, \tag{3.57}$$

whereas when $\gamma_i \gg \gamma_H$, the validity range extends to a lower magnetic field regime, $\frac{A}{N\gamma_i} \lesssim B \lesssim \frac{A}{\sqrt{N}\gamma_i}$. To physically understand this difference in N-dependence, we note that the expansion is controlled by the size of hyperfine-induced fluctuations $\delta\omega_{\text{rms}}$ relative to the relevant fast oscillation frequency ω, and subleading terms can be neglected when

$$\frac{\delta\omega_{\text{rms}}}{\omega} \ll 1. \tag{3.58}$$

More specifically, if the fast frequency is $\omega \sim \gamma_i B$, the hyperfine field acting on each precessing nuclear spin is of order $\delta\omega_{\text{rms}} \sim A/N$, leading to

$$\frac{\delta\omega_{\text{rms}}}{\omega} \sim \frac{A}{NB\gamma_i}, \quad \gamma_i \gg \gamma_H. \tag{3.59}$$

Otherwise, if $\omega \sim \gamma_H B$, the hole spin experiences a typical hyperfine field on the order of $\delta\omega_{\text{rms}} \sim A/\sqrt{N}$ from averaging over nuclear spin configurations, such that

$$\frac{\delta\omega_{\text{rms}}}{\omega} \sim \frac{A}{\sqrt{N}B\gamma_H}, \quad \gamma_H \gg \gamma_i. \tag{3.60}$$

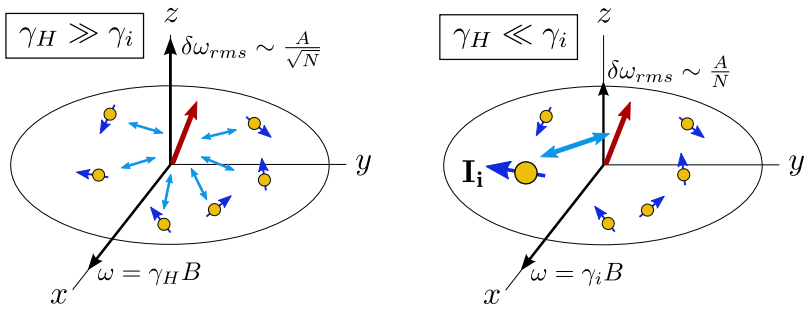

Figure 3–7: (Color online) Comparison of the relative size of fluctuations $\delta\omega_{\rm rms}/\omega$ between the two cases: $\gamma_H \gg \gamma_i$ and $\gamma_H \ll \gamma_i$. When the fast oscillation frequency is $\omega \sim \gamma_H B$, the hyperfine coupling strength felt by the hole spin results from a sum over all nuclear spins. However, if the fast frequency is $\omega \sim \gamma_i B$, each nuclear spin feels a coupling strength of $\sim A/N$ from the hole spin.

Fig. 3–7 illustrates the contrast between the two cases, and table 3–2 summarizes the parameters relevant in determining the validity of the Magnus expansion.

	$\gamma_H \gg \gamma_i$	$\gamma_H \ll \gamma_i < \frac{A}{B\sqrt{N}}$	$\gamma_H \ll \frac{A}{B\sqrt{N}} < \gamma_i$
ω	$\sim B\gamma_H$	$\sim B\gamma_i$	$\sim B\gamma_i$
$\delta\omega_{\rm rms}$	$\sim A/\sqrt{N}$	$\sim A/N$	$\sim A/N$
$\tau_{\rm max}$	$\sim \omega/\delta\omega_{\rm rms}^2$	$\sim \omega/\delta\omega_{\rm rms}^2$	$\sim \frac{1}{A}(\omega/\delta\omega_{\rm rms})^3$

Table 3–2: Summary of the conditions for validity of the Magnus expansion. In each of the three cases, the approximation scheme is valid for $\delta\omega_{\rm rms}/\omega \ll 1$ and for $t < \tau_{\rm max}$.

Additionally, subleading terms which grow with τ cause non negligible dephasing when they become of order unity at $\tau \sim \tau_{\rm max}$. As shown in Appendix C, we find that, in the motional averaging regime, progressively higher-order terms become relevant at a progressively shorter time, saturating at

$$\tau_{\rm max} \sim \frac{\omega}{\delta\omega_{\rm rms}^2}. \tag{3.61}$$

However, for the special case $\gamma_i \gg \gamma_H$ there is an intermediate regime, $\delta\omega_{\rm rms} \ll \gamma_i B \ll \sqrt{N}\delta\omega_{\rm rms}$, in which low-order subleading terms dominate, giving

$$\tau_{\rm max} \sim \frac{1}{A}\left(\frac{\omega}{\delta\omega_{\rm rms}}\right)^3. \tag{3.62}$$

There is no such intermediate regime when $\gamma_H \gg \gamma_i$. The upshot of this analysis is that $\omega > \delta\omega_{\rm rms}$ (i.e. $\gamma_i B > A/N$) can be easily satisfied for $\gamma_i \gg \gamma_H$, even outside of the motional-averaging regime, giving the good agreement shown in Fig. 3–4. In contrast, when $\gamma_H \gg \gamma_i$, the Magnus expansion is guaranteed to provide an accurate description only in the motional averaging regime and for $\tau \lesssim \tau_{\rm max}$.

3.4 Free-induction dynamics

In the absence of refocusing spin-echo pulses, we expect additional dephasing due to slowly-varying fluctuations in the nuclear field. To obtain the exact free-induction spin dynamics in the $g_\perp \simeq 0$ limit, we again follow the procedure outlined in Sec. 3.2, which yields a solution of the form

$$\frac{\langle S_x(\tau)\rangle}{\langle S_x(0)\rangle} = {\rm Re}\prod_{k=1}^{N} {\rm Tr}\left\{\left(E_k R_k E_k^{-1} R_k^{-1}\right)\rho_k\right\}, \tag{3.63}$$

where all the symbols are defined in Sec. 3.2. Eq.(3.63) is plotted in Fig. 3–8 for a range of magnetic fields, demonstrating the same motional averaging effect due to fast precession of the nuclear spins at large B. Below the motional averaging regime, however, whereas the echo sequence previously extended coherence times by removing the slow nuclear-field fluctuations, here the initial decay time τ_0 is limited by static nuclear-field fluctuations and has no B dependence. A

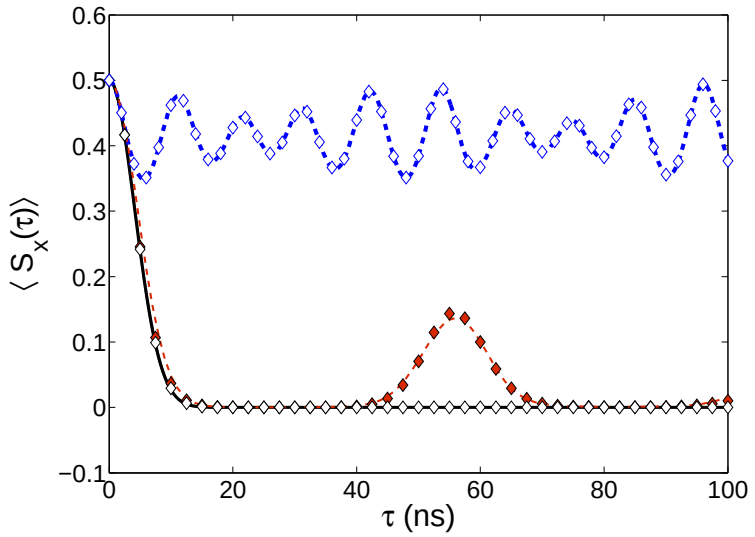

Figure 3–8: (Color online) Exact free-induction dynamics [Eq. (3.63)] with $B = 1$ T (black solid line), $B = 2$ T (thin red dashed line), and $B = 10$ T (thick blue dashed line), showing motional averaging at large magnetic fields. Markers represent the approximate solution [Eq.(3.66)], and all other parameters are given in Fig. 3–4.

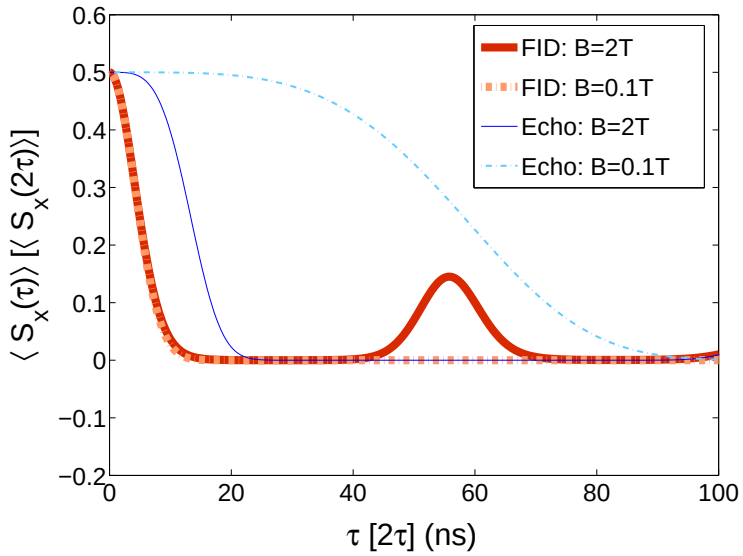

Figure 3–9: (Color online) Comparison of exact free-induction [Eq. (3.63)] and spin echo [Eq. (3.15)] dynamics for magnetic fields below the motional averaging regime, where spin echo extends coherence times by reversing slowly-varying fluctuations from nuclear-spin precession. Parameters used are the same as in Fig. 3–4, except for the values of B, which are indicated in the legend.

comparison between free-induction and echo dynamics at low magnetic fields is shown in Fig. 3–9.

When $g_\perp \neq 0$, the method described in Sec. 3.3 also yields the approximate free-induction solution, provided we replace the time-evolution operator by its free-induction analogue $\tilde{U}(\tau)$, which is given by

$$\tilde{U}(\tau) = \mathcal{T} e^{-i\int_0^\tau dt \tilde{H}(t)} = e^{-iH_M(\tau)}. \tag{3.64}$$

The free-induction solution is given in terms of $h^{\gamma\delta}_{\mathrm{FID}}(\tau)$, with

$$h^{\gamma\delta}_{\mathrm{FID}}(\tau) = \sum_{k,\alpha=y,z} A_k^2 g^{\alpha\gamma}_{k,\mathrm{FID}}(\tau) g^{\alpha\delta}_{k,\mathrm{FID}}(\tau) \frac{I_k(I_k+1)}{3}, \tag{3.65}$$

where $g^{\alpha\beta}_{k,\mathrm{FID}}(\tau)$ are defined in Eqs. (B.1)-(B.4) of Appendix B. For instance, free-induction coherence dynamics along x is given by

$$\frac{\langle S_x(\tau)\rangle}{\langle S_x(0)\rangle} \simeq e^{-\bar{h}_{\mathrm{FID}}(\tau)}, \tag{3.66}$$

with $\bar{h}_{\mathrm{FID}}(\tau) = \frac{1}{2}\left[h^{yy}_{\mathrm{FID}}(\tau) + h^{zz}_{\mathrm{FID}}(\tau)\right]$.

Free-induction dynamics in an in-plane magnetic field and with $\gamma_i = 0$ has been calculated for the z-component of the hole spin, $S_z(\tau)$, to be a power-law decay [12] given by

$$\langle S_z(\tau)\rangle \simeq \frac{\cos\left(\gamma_H B\tau + \frac{1}{2}\arctan\left(\tau/\tau_\parallel\right)\right)}{2\left(1+\left(\tau/\tau_\parallel\right)^2\right)^{1/4}}, \tag{3.67}$$

where $\tau_\parallel = \gamma_H B/\langle (h_z)^2\rangle$. Comparison with the solution obtained through the Magnus expansion exemplifies an instance where the Magnus expansion fails for $\tau \gtrsim \tau_{\max}$, in contrast to the $g_\perp = 0$ case discussed above where the approximate solution remains valid at time scales $\tau \gg \tau_{\max}$. At leading order in the Magnus expansion, $\langle S_z(\tau)\rangle$ shows no decay; we therefore include the subleading order in the expansion, and plot the resulting spin dynamics in Fig. 3–10 alongside Eq.(3.67). From table 3–2, an order-of-magnitude estimate gives $\tau_{\max} \sim 100$ ns, consistent with the time scale beyond which the Magnus expansion seems to fail in Fig. 3–10.

3.5 Conclusion

In conclusion, we have calculated the spin-echo dynamics of a single heavy-hole in a quantum dot, in the limit of weak strain. Following a discussion of the behaviour of all spin components, we show that the spin purity is maximized for

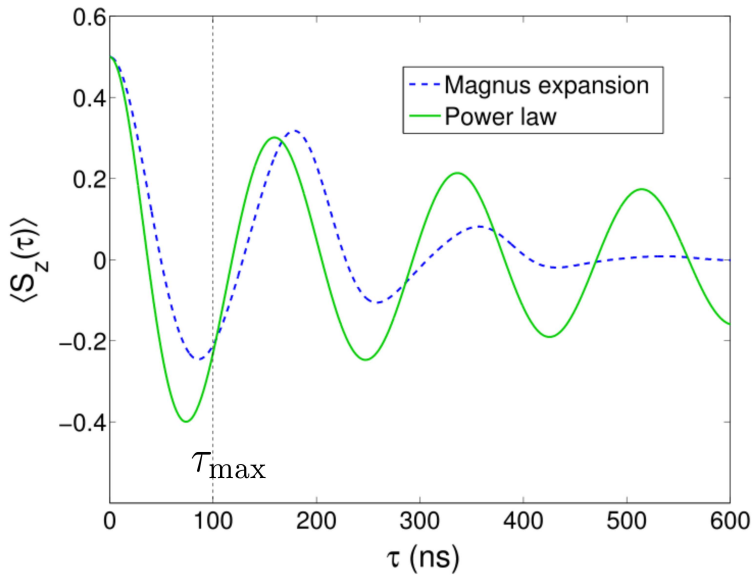

Figure 3–10: (Color online) Comparison of the Magnus expansion solution (dotted blue curve) for $\langle S_z(\tau)\rangle$ with the previously established result (solid green curve) [12], with $B = 10$ mT, $N = 6.5 \times 10^5$, $\gamma_i = 0$ for all nuclear species and $g_\perp = 0.04$. The Magnus expansion fails for $\tau \gtrsim 100$ ns, consistent with our estimate for $\tau_{\max}$ from table 3–2.

initialization along the fluctuating Overhauser field, while one might naively expect spin purity to be highest for preparation in a Zeeman eigenstate.

We also investigate the validity regimes of the Magnus expansion and of the Gaussian approximation in terms of relevant parameters (A, N, B, γ_i and γ_H), revealing a difference in N-dependence for the two cases ($\gamma_i \gg \gamma_H$ or $\gamma_i \ll \gamma_H$) due to the hole spin experiencing a hyperfine interaction strength which is averaged over the nuclear spins.

CHAPTER 4
Conclusion

In this thesis we have presented further evidence of the hole spin's robustness for quantum information processing. We have calculated the coherence dynamics of a single heavy-hole spin in a quantum dot under spin echo, assuming a flat, strain-free dot. Accounting for rapid precession due to the hole and nuclear Zeeman terms, we developed an approximation scheme based on the Magnus expansion, an average-Hamiltonian theory which yields fast convergence for rapidly-oscillating systems. We considered an in-plane magnetic field $\mathbf{B} = B\hat{x}$ which drives the system into a motional averaging regime whenever $B \gtrsim A/\gamma\sqrt{N}$, with $\gamma = \max\{\gamma_i, \gamma_H\}$ (where γ_i is the nuclear gyromagnetic ratio and γ_H is the in-plane hole gyromagnetic ratio). In the motional averaging regime, the decay in the hole spin-echo envelope signal can be completely suppressed for magnetic fields of $B \gtrsim 10$T for $\gamma_i \gg \gamma_H$ and $N = 10^4$ (or equivalently, $B \gtrsim 1$T for $N = 10^6$), and at even lower fields when $\gamma_H \gg \gamma_i$. For $\gamma_i \gg \gamma_H$, the Magnus expansion further yields an accurate description in the range $A/\gamma_i N \lesssim B \lesssim A/\gamma_i\sqrt{N}$, where we predicted a shortening of coherence times with increasing B.

The hole spin dynamics are also highly anisotropic, depending on the spin component of interest as well as the π-rotation axis. We showed, at the end of chapter 2, that initializing along the x-axis instead of the y-axis and choosing π-pulses about x instead of z would suppress the effects of electric-field fluctuations

and lead to extremely long decay timescales ($\tau_D \simeq 20$s using the parameters from Ref. [2]), if electric-field fluctuations were the only relevant source of decoherence. The alternate geometry we proposed would allow for measurements of the intrinsic hyperfine-limited coherence dynamics, rather than the dynamics from extrinsic effects such as charge noise due to device imperfections.

Another major consequence of the anisotropy can be seen in calculations of the spin purity, a quantity characterizing the spin-qubit polarization which can be extracted after the system has been entangled with the environment for some time t. Expressing the spin-purity in terms of eigenfunctions of the Liouvillian, we found it to be maximized when the hole spin is initialized in the z-direction, along the hyperfine-induced fluctuations. While one might naively expect the purity to be best preserved for initialization along the external magnetic field and perpendicular to the fluctuations, our results show that the opposite is true. Intuitively, since the z-component of the hole spin does not precess about the Overhauser field, its evolution would not be affected by hyperfine-induced fluctuations, whereas the x-component would be affected.

To further characterize the decoherence mechanisms specific to single hole spins in semiconductor quantum dots, a closer investigation of the effects of charge noise on coherence dynamics is needed. Electric-field-induced fluctuations in the hole spin Zeeman energy are currently thought to limit coherence times in experiments carried out in self-assembled quantum dots [2, 3]. While we have estimated the decay time attributed to charge fluctuations for a specific case in

Sec. 2.5, a generalized phenomenological calculation of combined hyperfine and charge noise effects is still under way.

A major correction to the Ising hyperfine Hamiltonian has been proposed to explain recent experimental results where the ratio of hole to electron hyperfine constants was measured to have opposite signs for cations (gallium, indium) and anions (phosphorous, arsenic) [39]. By including a d-orbital contribution in addition to the p-orbitals in the hole wavefunction, the authors of Ref. [39] were able to account for the measured sign difference in the hyperfine constants of various nuclear species. The same theory was also used to estimate a d-orbital contribution of about 20% [39], leading to significant off-diagonal elements in the hole hyperfine Hamiltonian, terms which introduce an additional spin-flip mechanism for hole-spin decoherence. However, a previous experiment has shown that the optical pumping scheme used to initialize the hole spin is effective even at zero applied magnetic field [30], implying that even when the hole spin-up and spin-down states are not split by the Zeeman energy, the hyperfine coupling does not mix them. We are therefore currently considering alternative mechanisms which could explain the difference in sign between the hyperfine constants of anions and cations.

Appendix A: Magnus expansion and Gaussian approximation

Given a periodic Hamiltonian $H(t)$, the Magnus expansion allows us to rewrite the time-evolution operator $U(t)$ as a series expansion:

$$U(t) = \mathcal{T} e^{-i\int_0^t dt' H(t')} \equiv e^{-iH_M(t)}, \tag{A.1}$$

where $H_M(t) = \sum_{i=1}^{\inf} H^{(i)}(t)$.

The first few terms in $H_M(t)$ are given by

$$H^{(0)}(t) = \int_0^t H(t_1) dt_1 \tag{A.2}$$

$$H^{(1)}(t) = -\frac{i}{2}\int_0^t \int_0^{t_2} [H(t_2), H(t_1)]\, dt_1 dt_2 \tag{A.3}$$

$$H^{(2)}(t) = -\frac{1}{6}\int_0^t \int_0^{t_3} \int_0^{t_2} [H(t_3), [H(t_2), H(t_1)]] + [H(t_1), [H(t_2), H(t_3)]] dt_1 dt_2 dt_3. \tag{A.4}$$

To derive the moment expansion in Eqs.(2.6) and (3.24), we begin by considering the general form of $H_M(t)$:

$$H_M(t) = \sum_{k,j} h_k^j(t) S^j = \mathbf{h_k}(t) \cdot \mathbf{S} \tag{A.5}$$

$$\mathbf{h_k}(t) = \mathbf{I_k} \cdot \overleftrightarrow{g_k} \tag{A.6}$$

where the g_k's are functions of t and are proportional to $1/\gamma$, with $\gamma = \sqrt{\gamma_i^2 + \gamma_H^2}$.

We assume that the nuclear bath is in an infinite temperature thermal state such that the nuclear spins are unpolarized ($\langle I_k^x \rangle = \langle I_k^y \rangle = \langle I_k^z \rangle = 0$) and uncorrelated ($\langle I_k^\alpha I_{k'}^\beta \rangle \propto \delta_{k,k'}$).

Taylor expand $e^{iL_M} S_\alpha$ and take the average over nuclear spins first:

$$\begin{aligned}
\langle e^{iL_M} S_\alpha \rangle &= \left\langle 1 + iL_M - \frac{1}{2} L_M^2 - \frac{i}{3!} L_M^3 + ... \right\rangle \qquad \text{(A.7)} \\
&= \left\langle 1 + i \sum_{k,j} \left[h_k^j S_j, S_+ \right] - \frac{1}{2} \sum_{k,k',j,j'} \left[h_{k'}^{j'} S_{j'}, \left[h_k^j S_j, S_+ \right] \right] \right. \\
&\quad \left. - \frac{i}{3!} \sum \left[h_{k''}^{j''} S_{j''}, \left[h_{k'}^{j'} S_{j'}, \left[h_k^j S_j, S_+ \right] \right] \right] + ... \right\rangle \\
&\simeq \left\langle 1 + i \sum_{k,j} \left\langle h_k^j \right\rangle_I [S_j, S_+] - \frac{1}{2} \sum \left\langle h_{k'}^{j'} h_k^j \right\rangle_I [S_{j'}, [S_j, S_+]] \right. \\
&\quad \left. - \frac{i}{3!} \sum \left\langle h_{k''}^{j''} h_{k'}^{j'} h_k^j \right\rangle_I [S_{j''}, [S_{j'}, [S_j, S_+]]] + ... \right\rangle_S
\end{aligned}$$

where on the last line, we neglected all the terms involving at least one commutator of h_k^j and $h_{k'}^{j'}$ since $\left[h_{k'}^{j'} S_{j'}, h_k^j S_j \right] \propto \delta_{k,k'}$. To justify this, consider that as a consequence of the above assumptions, the magnitude of each term depends on the number of h_k^j's (each h_k^j contributes a factor of $A/N\gamma$) and on the number of independent indices to sum over (each sum over k contributes a factor of N). The magnitude of the n^{th} moment is thus (approximately) calculated as

$$\begin{aligned}
&\sum_k \langle (h_k)^n \rangle \propto \sum_k \left(\frac{A_k}{\gamma} \right)^n \\
&\simeq \int_0^\infty dk \left(\frac{A e^{-k/N}}{N\gamma} \right)^n = \frac{N}{n} \left(\frac{A}{N\gamma} \right)^n . \qquad \text{(A.8)}
\end{aligned}$$

A commutator such as $\left[h_{k'}^{j'}, h_k^j\right]$ reduces the number of independent nuclear spin indices available for averaging over, thus terms involving commutators will be suppressed by factors of $1/N$ relative to those with no commutators. Furthermore, the even moments can be factored into pairs such that the $(2n)^{th}$ moment will be $\propto A^{2n}/\gamma^{2n}N^n$ whereas the odd moments vanish.

$$\left\langle \left(\sum_k h_k^j \right)^{2n} \right\rangle_I \simeq a_n \sum \left\langle h_{k_1}^{j_1} h_{k_1}^{j_1'} \right\rangle \left\langle h_{k_2}^{j_2} h_{k_2}^{j_2'} \right\rangle ... \left\langle h_{k_n}^{j_n} h_{k_n}^{j_n'} \right\rangle \tag{A.9}$$

where a_n is the number of unique ways to group $2n$ terms into n pairs.

$$a_n = \frac{1}{n!} \binom{2n}{2} \binom{2n-2}{2} \binom{2n-4}{2} ... \binom{4}{2} \tag{A.10}$$

$$= \frac{1}{n!} \frac{(2n)!}{2^n} \tag{A.11}$$

Plugging equations (A.9) and (A.11) back into the Taylor series of equation (A.8) and then defining the Liouvillian acting only on the hole spin, L_S^j, as $L_S^j \mathcal{O}_\mathcal{S} = [S^j, \mathcal{O}_\mathcal{S}]$, we get:

$$\begin{aligned}
\langle S_\alpha(t) \rangle &\simeq \left\langle \sum_n \frac{i^{2n}}{(2n)!} \left\langle \left(\sum_{k,j} h_k^j L_S^j \right)^{2n} \right\rangle_I S_\alpha \right\rangle_S \\
&= \left\langle \sum_n \frac{(-1)^n}{(2n)!} a_n \left(\sum_{k,j,j'} \left\langle h_k^j h_k^{j'} \right\rangle_I L_S^j L_S^{j'} \right)^n S_\alpha \right\rangle_S \\
&= \left\langle \sum_n \frac{1}{n!} \left(-\frac{1}{2} \sum_{k,j,j'} \left\langle h_k^j h_k^{j'} \right\rangle_I L_S^j L_S^{j'} \right)^n S_\alpha \right\rangle_S \\
&= \left\langle \exp\left\{ -\frac{1}{2} \left\langle L_M^2 \right\rangle_I \right\} S_\alpha \right\rangle_S
\end{aligned} \tag{A.12}$$

Appendix B: Approximate solution ($g_\perp \neq 0$)

Free induction:

$$g^{yy}_{k,\mathrm{FID}}(\tau) = \frac{1}{\omega_{k-}}\sin(\omega_{k-}\tau) - \frac{1}{\omega_{k+}}\sin(\omega_{k+}\tau) \tag{B.1}$$

$$g^{zz}_{k,\mathrm{FID}}(\tau) = \frac{1}{\omega_{k-}}\sin(\omega_{k-}\tau) + \frac{1}{\omega_{k+}}\sin(\omega_{k+}\tau) \tag{B.2}$$

$$g^{yz}_{k,\mathrm{FID}}(\tau) = \frac{2B\gamma_k}{\omega_{k+}\omega_{k-}} - \frac{1}{\omega_{k-}}\cos(\omega_{k-}\tau) - \frac{1}{\omega_{k+}}\cos(\omega_{k+}\tau) \tag{B.3}$$

$$g^{zy}_{k,\mathrm{FID}}(\tau) = \frac{1}{\omega_{k-}}\cos(\omega_{k-}\tau) - \frac{1}{\omega_{k+}}\cos(\omega_{k+}\tau) - \frac{2b}{\omega_{k+}\omega_{k-}} \tag{B.4}$$

Spin echo:

$$g^{yy}_{k}(2\tau) = \frac{1}{\omega_{k+}}\left[\sin(2\omega_{k+}\tau) - 2\sin(\omega_{k+}\tau)\right] - \frac{1}{\omega_{k-}}\left[\sin(2\omega_{k-}\tau) - 2\sin(\omega_{k-}\tau)\right] \tag{B.5}$$

$$g^{zz}_{k}(2\tau) = \frac{1}{\omega_{k+}}\left[2\sin(\omega_{k+}\tau) - \sin(2\omega_{k+}\tau)\right] + \frac{1}{\omega_{k-}}\left[2\sin(\omega_{k-}\tau) - \sin(2\omega_{k-}\tau)\right] \tag{B.6}$$

$$g^{yz}_{k}(2\tau) = \frac{1}{\omega_{k+}}\left[\cos(2\omega_{k+}\tau) - 2\cos(\omega_{k+}\tau)\right] + \frac{1}{\omega_{k-}}\left[\cos(2\omega_{k-}\tau) - 2\cos(\omega_{k-}\tau)\right] + \frac{2B\gamma_k}{\omega_{k+}\omega_{k-}} \tag{B.7}$$

$$g^{zy}_{k}(2\tau) = \frac{1}{\omega_{k+}}\left[\cos(2\omega_{k+}\tau) - 2\cos(\omega_{k+}\tau)\right] - \frac{1}{\omega_{k-}}\left[\cos(2\omega_{k-}\tau) - 2\cos(\omega_{k-}\tau)\right] - \frac{2b}{\omega_{k+}\omega_{k-}} \tag{B.8}$$

$$\omega_{k+} = B(\gamma_k + \gamma_H) \tag{B.9}$$

$$\omega_{k-} = B(\gamma_k - \gamma_H) \tag{B.10}$$

Appendix C: Approximations and range of validity

$$H^{(n)}(2\tau) = H^{(n)}_{\rm bnd}(2\tau) + H^{(n)}_{\rm unb}(2\tau), \quad n = 1, 2, ... \tag{C.1}$$

Meanwhile, the leading-order term, $H^{(0)}(2\tau)$, is bounded so that

$$H^{(0)}(2\tau) = H^{(0)}_{\rm bnd}(2\tau). \tag{C.2}$$

The bounded contributions of the lowest subleading terms in the Liouvillian $\langle L^2_M(2\tau)\rangle_I$ can be neglected if their amplitudes are small compared to the amplitude of the leading-order term:

$$\left\| \left(H^{(0)}(2\tau)\right)^2 \right\| \gg \left\| H^{(0)}(2\tau) H^{(2)}_{\rm bnd}(2\tau) \right\|, \left\| \left(H^{(1)}_{\rm bnd}(2\tau)\right)^2 \right\|. \tag{C.3}$$

In terms of the parameters A, N, B, γ_i, and γ_H, the above condition for the validity of the leading-order Liouvillian can be rewritten as

$$\frac{A}{NB\gamma_i} \ll 1, \qquad \text{if } \gamma_i \gg \gamma_H \tag{C.4}$$

$$\frac{A}{\sqrt{N}B\gamma_H} \ll 1, \qquad \text{if } \gamma_H \gg \gamma_i \tag{C.5}$$

Case 1: $\gamma_k \ll \gamma_H$

$$\tilde{H}(t) \simeq h_z \tilde{S}_z(t) \tag{C.6}$$

with h_z and $\tilde{S}_z(t)$ as defined in sections 3.1 and 3.3. The higher order terms in the Magnus expansion are then estimated as:

$$H^{(n)}(t) \sim \int_0^t \int_0^{t_{n+1}} \dots \int_0^{t_2} \left[\tilde{H}_{n+1}, \dots [\tilde{H}_2, \tilde{H}_1] \dots\right] dt_1 \dots dt_{n+1} \tag{C.7}$$

$$\sim h_z^{n+1} \int_0^t \int_0^{t_{n+1}} \dots \int_0^{t_2} \left[\tilde{S}_{n+1}, \dots [\tilde{S}_2, \tilde{S}_1] \dots\right] dt_1 \dots dt_{n+1} \tag{C.8}$$

$$\sim h_z^{n+1} \left(\frac{f(t)}{(B\gamma_H)^{n+1}} + \dots + \left(\frac{t}{B\gamma_H}\right)^{\frac{n+1}{2}} f'(t) \right) \text{ if n is odd} \tag{C.9}$$

$$\sim h_z^{n+1} \left(\frac{f(t)}{(B\gamma_H)^{n+1}} + \dots + \frac{t^{n/2}}{(B\gamma_H)^{\frac{n}{2}+1}} f'(t) \right) \text{ if n is even} \tag{C.10}$$

where $H_i = H(t_i)$ and $\tilde{S}_i = \tilde{S}(t_i)$, and $f(t)$ and $f'(t)$ are factors (constants, sinusoidal functions, etc.) of order unity. Since the odd moments $\langle h_z^{2i+1} \rangle = 0$, only odd-odd and even-even terms contribute to $\langle S_\alpha(t) \rangle$. From the first term in Eq. (C.9) and in Eq. (C.10), we see that oscillating terms in higher orders are suppressed by a factor:

$$\frac{||H^{(i+2)} H^{(j)}||}{||H^{(i)} H^{(j)}||} \sim \frac{\langle h_z^2 \rangle}{(B\gamma_H)^2} = \left(\frac{\delta\omega_{\text{rms}}}{\omega_H}\right) \tag{C.11}$$

When the term which grows fastest in t becomes of order 1, the Magnus expansion may fail. Thus the last term in Eqs. (C.9) and (C.10) tells us the time $\tau_{\max}$ up to which the Magnus expansion should be valid. For the odd-odd terms,

$$\tau_{\max} \sim \frac{B\gamma_H}{\langle h_z^2 \rangle}. \tag{C.12}$$

For an even-even term of the form $H^{(2i)} H^{(2j)}$, and with $m = i + j$,

$$\tau_{\max} \sim \frac{(B\gamma_H)^{\frac{m+2}{m}}}{(A/\sqrt{N})^{\frac{2m+2}{m}}} = \frac{1}{\delta\omega_{\text{rms}}} \left(\frac{B\gamma_H}{\delta\omega_{\text{rms}}}\right)^{1+\frac{2}{m}} \tag{C.13}$$

We find the smallest $\tau_{\max}$ by taking the limit as $m \to \infty$, such that $\tau_{\max} \to \frac{B\gamma_H}{\langle h_z^2 \rangle}$, just like for the odd-odd terms.

Case 2: $\gamma_H \ll \gamma_k$

$$\tilde{H}(t) \simeq \tilde{h}_z(t) S_z \tag{C.14}$$

The odd terms $H^{2n+1} \sim S_z^{2n+2} \propto I_S$, so

$$L^{(2n+1)} S_\alpha = [H^{(2n+1)}, S_\alpha] \equiv 0 \tag{C.15}$$

Only even-even terms are left:

$$\left\langle \left[H^{(2i)}, \left[H^{(2j)}, \tilde{S}_\alpha \right] \right] \right\rangle \sim \sum_k A_k^{2(i+j+1)} \frac{\tau_{\max}^{i+j}}{(\gamma_k B)^{i+j+2}} \tag{C.16}$$

$$\tau_{\max} \sim \frac{\gamma_k B}{\delta\omega_{\rm rms}^2} \left(\frac{1}{N} \left(\frac{\gamma_k B}{\delta\omega_{\rm rms}} \right)^2 \right)^{1/(i+j)} \tag{C.17}$$

If $\frac{1}{N} \left(\frac{\gamma_k B}{\delta\omega_{\rm rms}} \right)^2 \ll 1$, maximize $1/m$:

$$\tau_{\max} \sim \frac{1}{A} \left(\frac{\gamma_k B}{\delta\omega_{\rm rms}} \right)^3 \tag{C.18}$$

If $\frac{1}{N} \left(\frac{\gamma_k B}{\delta\omega_{\rm rms}} \right)^2 \gg 1$, minimize $1/m$:

$$\tau_{\max} \sim \frac{\gamma_k B}{\delta\omega_{\rm rms}^2} \tag{C.19}$$

References

[1] X. J. Wang, S. Chesi, and W. A. Coish. Spin-echo dynamics of a heavy hole in a quantum dot. *Phys. Rev. Lett.*, 109:237601, 2012.

[2] K. De Greve, P.L. McMahon, D. Press, T.D. Ladd, D. Bisping, C. Schneider, M. Kamp, L. Worschech, S. Hoefling, A. Forchel, and Y. Yamamoto. Coherent control and suppressed nuclear feedback of a single quantum dot hole qubit. *Nature Phys.*, 7:872–878, 2011.

[3] Alex Greilich, Samuel G. Carter, Danny Kim, Allan S. Bracker, and Daniel Gammon. Optical control of one and two hole spins in interacting quantum dots. *Nature Photonics*, 5:702–708, 2011.

[4] Igor Zutic, Jaroslav Fabian, and S. Das Sarma. Spintronics: Fundamentals and applications. *Rev. Mod. Phys.*, 76:323–410, 2004.

[5] L. P. Kouwenhoven, D. G. Austing, and S. Tarucha. Few-electron quantum dots. *Rep. Prog. Phys.*, 64(6):701, 2001.

[6] Daniel Loss and David P. DiVincenzo. Quantum computation with quantum dots. *Phys. Rev. A*, 57:120–126, 1998.

[7] R. Hanson, L. P. Kouwenhoven, J. R. Petta, S. Tarucha, and L. M. K. Vandersypen. Spins in few-electron quantum dots. *Rev. Mod. Phys.*, 79:1217–1265, 2007.

[8] W. A. Coish and J. Baugh. Nuclear spins in nanostructures. *Phys. Status Solidi B*, 246(10):2203–2215, 2009.

[9] A.V. Khaetskii, D. Loss, and L. Glazman. Electron spin decoherence in quantum dots due to interaction with nuclei. *Phys. Rev. Lett.*, 88(18):186802, 2002.

[10] IA Merkulov, A.L. Efros, and M. Rosen. Electron spin relaxation by nuclei in semiconductor quantum dots. *Phys. Rev. B*, 65(20):205309, 2002.

[11] W. A. Coish and Daniel Loss. Hyperfine interaction in a quantum dot: Non-markovian electron spin dynamics. *Phys. Rev. B*, 70:195340, 2004.

[12] Jan Fischer, W. A. Coish, D. V. Bulaev, and Daniel Loss. Spin decoherence of a heavy hole coupled to nuclear spins in a quantum dot. *Phys. Rev. B*, 78:155329, 2008.

[13] L Jacak, Pawel Hawrylak, and Arkadiusz Wjs. *Quantum dots*. Springer, Berlin, 1998.

[14] B. J. Riel. An introduction to self-assembled quantum dots. *Am. J. Phys.*, 76:750, 2008.

[15] JR Petta, AC Johnson, JM Taylor, EA Laird, A. Yacoby, MD Lukin, CM Marcus, MP Hanson, and AC Gossard. Coherent manipulation of coupled electron spins in semiconductor quantum dots. *Science*, 309(5744):2180–2184, 2005.

[16] M. D. Shulman, O. E. Dial, S. P. Harvey, H. Bluhm, V. Umansky, and A. Yacoby. Demonstration of entanglement of electrostatically coupled singlet-triplet qubits. *Science*, 336(6078):202–205, 2012.

[17] Alexander V. Khaetskii and Yuli V. Nazarov. Spin relaxation in semiconductor quantum dots. *Phys. Rev. B*, 61:1263912642, 2000.

[18] R. Winkler. *Spin-orbit Coupling Effects in Two-Dimensional Electron and Hole Systems*. Springer, Berlin, 2003.

[19] B. I. Halperin, Ady Stern, Yuval Oreg, J. N. H. J. Cremers, J. A. Folk, and C. M. Marcus. Zeeman energy and spin relaxation in a one-electron quantum dot. *Phys. Rev. Lett.*, 91(19):196802, 2003.

[20] I. L. Aleiner and Vladimir I. Fal'ko. Spin-orbit coupling effects on quantum transport in lateral semiconductor dots. *Phys. Rev. Lett.*, 87:256801, 2001.

[21] D. M. Zumbhl, J. B. Miller, C. M. Marcus, K. Campman, and A. C. Gossard. Spin-orbit coupling, antilocalization, and parallel magnetic fields in quantum dots. *Phys. Rev. Lett.*, 89:276803, 2002.

[22] Alexander V. Khaetskii and Yuli V. Nazarov. Spin-flip transitions between zeeman sublevels in semiconductor quantum dots. *Phys. Rev. B*, 64:125316, 2001.

[23] Toshimasa Fujisawa, David Guy Austing, Yasuhiro Tokura, Yoshiro Hirayama, and Seigo Tarucha. Allowed and forbidden transitions in artificial hydrogen and helium atoms. *Nature*, 419:278, 2002.

[24] R. Hanson, B. Witkamp, L. M. K. Vandersypen, L. H. Willems van Beveren, J. M. Elzerman, and L. P. Kouwenhoven. Zeeman energy and spin relaxation in a one-electron quantum dot. *Phys. Rev. Lett.*, 91(19):196802, 2003.

[25] J. M. Elzerman, R. Hanson, L. H. Willems van Beveren, B. Witkamp, L. M. K. Vandersypen, L. P. Kouwenhoven, Yoshiro Hirayama, and Seigo Tarucha. Single-shot read-out of an individual electron spin in a quantum dot. *Nature*, 430:431, 2004.

[26] S. Amasha, K. MacLean, Iuliana P. Radu, D. M. Zumbhl, M. A. Kastner, M. P. Hanson, and A. C. Gossard. Electrical control of spin relaxation in a quantum dot. *Phys. Rev. Lett.*, 100:046803, 2008.

[27] Denis V. Bulaev and Daniel Loss. Spin relaxation and decoherence of holes in quantum dots. *Phys. Rev. Lett.*, 95:076805, 2005.

[28] Mircea Trif, Pascal Simon, and Daniel Loss. Relaxation of hole spins in quantum dots via two-phonon processes. *Phys. Rev. Lett.*, 103:106601, 2009.

[29] D. Heiss, S. Schaeck, H. Huebl, M. Bichler, G. Abstreiter, and J. J. Finley. Observation of extremely slow hole spin relaxation in self-assembled quantum dots. *Phys. Rev. B*, 76:241306(R), 2007.

[30] BD Gerardot, D. Brunner, PA Dalgarno, P. Ohberg, S. Seidl, M. Kroner, K. Karrai, NG Stoltz, PM Petroff, and RJ Warburton. Optical pumping of a single hole spin in a quantum dot. *Nature*, 451:441–444, 2008.

[31] A. Abragam. *The Principles of Nuclear Magnetism*. Oxford University Press, Oxford, 1961.

[32] C. Testelin, F. Bernardot, B. Eble, and M. Chamarro. Holespin dephasing time associated with hyperfine interaction in quantum dots. *Phys. Rev. B*, 79:195440, 2009.

[33] A. M. Stoneham. *Theory of defects in solids*. Clarendon Press, Oxford, 1975.

[34] R. De Sousa and S. Das Sarma. Theory of nuclear-induced spectral diffusion: Spin decoherence of phosphorus donors in si and gaas quantum dots. *Phys. Rev. B*, 68(11):115322, 2003.

[35] Wang Yao, Ren-Bao Liu, and L. J. Sham. Theory of electron spin decoherence by interacting nuclear spins in a quantum dot. *Phys. Rev. B*, 74:195301, 2006.

[36] Jiangfeng Du, Xing Rong, Nan Zhao, Ya Wang, Jiahui Yang, and R. B. Liu. Preserving electron spin coherence in solids by optimal dynamical decoupling. *Nature*, 461:1265, 2009.

[37] G. de Lange, Z. H. Wang, D. Rist, V. V. Dobrovitski, and R. Hanson. Universal dynamical decoupling of a single solid-state spin from a spin bath. *Science*, 330:60, 2010.

[38] Jan Fischer and Daniel Loss. Hybridization and spin decoherence in heavy-hole quantum dots. *Phys. Rev. Lett.*, 105:266603, 2010.

[39] E. A. Chekhovich, M. M. Glazov, A. B. Krysa, M. Hopkinson, P. Senellart, A. Lematre, M. S. Skolnick, and A. I. Tartakovskii. Element-sensitive measurement of the holenuclear spin interaction in quantum dots. *Nature Physics*, 9:74–78, 2012.

[40] D. Brunner, Brian D. Gerardot, Paul A. Dalgarno, Gunter Wüst, Khaled Karrai, Nick G. Stoltz, Pierre M. Petroff, and Richard J. Warburton. A coherent single-hole spin in a semiconductor. *Science*, 325:70–72, 2009.

[41] E. A. Chekhovich, A. B. Krysa, M. S. Skolnick, and A. I. Tartakovskii. Direct measurement of the hole-nuclear spin interaction in single inp/gainp quantum dots using photoluminescence spectroscopy. *Phys. Rev. Lett.*, 106:027402, 2011.

[42] P. Fallahi, S. T. Yilmaz, and A. Imamoglu. Observation of heavy-hole hyperfine interaction in quantum dots. *Phys. Rev. Lett.*, 105:257402, 2010.

[43] T. M. Godden, J. H. Quilter, A. J. Ramsay, Yanwen Wu, P. Brereton, I. J. Luxmoore, J. Puebla, A. M. Fox, and M. S. Skolnick. Spin decoherence of a heavy hole coupled to nuclear spins in a quantum dot. *Phys. Rev. B*, 85:115310, 2012.

[44] Franziska Maier and Daniel Loss. Effect of strain on hyperfine-induced hole-spin decoherence in quantum dots. *Phys. Rev. B*, 85:195323, 2012.

[45] H. Bluhm, S. Foletti, I. Neder, M. Rudner, D. Mahalu, V. Umansky, and A. Yacoby. Dephasing time of gaas electron-spin qubits coupled to a nuclear bath exceeding 200 [thinsp][mu] s. *Nature Physics*, 7(2):109–113, 2010.

[46] Richard E. George, Wayne Witzel, H. Riemann, N. V. Abrosimov, N. Nötzel, Mike L. W. Thewalt, and John J. L. Morton. Electron spin coherence and electron nuclear double resonance of bi donors in natural si. *Phys. Rev. Lett.*, 105:067601, 2010.

[47] L. Childress, M.V.G. Dutt, JM Taylor, AS Zibrov, F. Jelezko, J. Wrachtrup, PR Hemmer, and MD Lukin. Coherent dynamics of coupled electron and nuclear spin qubits in diamond. *Science*, 314(5797):281–285, 2006.

[48] B. Eble, C. Testelin, P. Desfonds, F. Bernardot, A. Balocchi, T. Amand, A. Miard, A. Lemaitre, X. Marie, and M. Chamarro. Hole–nuclear spin interaction in quantum dots. *Phys. Rev. Lett.*, 102(14):146601, 2009.

[49] E. A. Chekhovich, A. B. Krysa, M. Hopkinson, P. Senellart, A. Lemaitre, M. S. Skolnick, and A. I. Tartakovskii. Isotope sensitive measurement of the hole-nuclear spin interaction in quantum dots. *arXiv:1109.0733*, 2011.

[50] T. M. Godden, J. H. Quilter, A. J. Ramsay, Yan Wen Wu, P. Brereton, S. J. Boyle, I. J. Luxmoore, J. Puebla-Nunez, A. M. Fox, and M. S. Skolnick. Coherent optical control of the spin of a single hole in an inas=gaas quantum dot. *Phys. Rev. Lett.*, 108:017402, 2012.

[51] N. A. Sinitsyn, Y. Li, SA Crooker, A. Saxena, and D. L. Smith. Role of nuclear quadrupole coupling on decoherence and relaxation of central spins in quantum dots. *arXiv:1206.3681*, 2012.

[52] T. Korn, M. Kugler, M. Griesbeck, R. Schulz, A. Wagner, M. Hirmer, C. Gerl, D. Schuh, W. Wegscheider, and C. Schüller. Engineering ultralong spin coherence in two-dimensional hole systems at low temperatures. *New Journal of Physics*, 12:043003, 2010.

[53] M. Matti Maricq. Application of average hamiltonian theory to the nmr of solids. *Phys. Rev. B*, 25(11):6622–6632, 1982.

[54] Łukasz Cywiński, Wayne M. Witzel, and S. Das Sarma. Electron spin dephasing due to hyperfine interactions with a nuclear spin bath. *Phys. Rev. Lett.*, 102:057601, 2009.

[55] L. G. Rowan, E. L. Hahn, and W. B. Mims. Electron-spin-echo envelope modulation. *Phys. Rev.*, 137:A61–A71, 1965.

[56] X. Marie, T. Amand, P. Le Jeune, M. Paillard, P. Renucci, LE Golub, VD Dymnikov, and EL Ivchenko. Hole spin quantum beats in quantum-well structures. *Phys. Rev. B*, 60:5811, 1999.

[57] J. R. Klauder and P. W. Anderson. Spectral diffusion decay in spin resonance experiments. *Phys. Rev.*, 125:912, 1962.

[58] W. M. Witzel, Rogerio de Sousa, and S. Das Sarma. Quantum theory of spectral-diffusion-induced electron spin decoherence. *Phys. Rev. B*, 72:161306(R), 2005.

[59] Felix Beaudoin and W. A. Coish. Enhanced hyperfine-induced spin dephasing in a magnetic-field gradient. *arXiv:1305.7506*, 2013.

[60] Tomaz Prosen and Thomas H. Seligman. Decoherence of spin echoes. *J. Phys. A:Math. Gen.*, 35:4707, 2002.

[61] S. Bravyi and A. Kitaev. Universal quantum computation with ideal clifford gates and noisy ancillas. *Phys. Rev. A*, 71:022316, 2005.